

# Prospects of detecting gamma-ray emission from galaxy clusters: cosmic rays and dark matter annihilations

Anders Pinzke<sup>1,\*</sup>, Christoph Pfrommer<sup>2,†</sup> and Lars Bergström<sup>3,‡</sup>

<sup>1</sup>*University of California - Santa Barbara, Department of Physics, CA 93106-9530, USA*

<sup>2</sup>*Heidelberg Institute for Theoretical Studies (HITS),*

*Schloss-Wolfsbrunnenuweg 33, DE - 69118 Heidelberg, Germany and*

<sup>3</sup>*The Oskar Klein Centre for Cosmoparticle Physics, Department of Physics, Stockholm University, AlbaNova University Center, SE - 106 91 Stockholm, Sweden*

(Dated: April 4, 2011)

... to be written...

PACS numbers: 95.35.+d, 95.85.Pw, 98.62.Gq, 98.65.-r, 98.70.Sa

## I. INTRODUCTION

Dark matter has been searched for in direct detection experiments [1], at accelerators [2–4] and also in indirect detection experiments looking for signals in the cosmic-ray spectra of antiprotons, positrons, neutrinos and all of the electromagnetic spectrum from radio waves to gamma rays [5]. So far, the improvements in direct detection sensitivity have put this method into focus, but the situation may change considerably the coming few years as the CERN LHC experiments collect data, and new gamma-ray detectors are being planned, such as the CTA [6]. In fact, it has recently been pointed out [7] that a dedicated ground-based gamma-ray detector would have potential that goes far beyond that of the other methods, depending on presently unknown parameters in the particle physics models for dark matter.

Among the astrophysical systems which will be very interesting to detect, and study, with coming gamma-ray detectors (Fermi, HESS, MAGIC, VERITAS, and eventually large detectors like CTA) belong galaxy clusters. The most promising directions in which to search for a gamma-ray annihilation signal (from the annihilation process itself, and also the accompanying bremsstrahlung and inverse Compton components coming from charged particles produced in the annihilations) are basically three:

1. The galactic centre (g.c.). This is where all numerical simulations of cold dark matter predict the highest density. However, the detailed dark matter density in the very central part is difficult to predict, due to a possibly very complicated interplay between baryons, dark matter, and the central galactic black hole. Also, it is a very crowded region with many gamma-ray sources like pulsars and other supernova remnants, which have to be subtracted from the data to extract the dark matter induced signal. In fact, there is a recent claim of an indication of a relatively light dark matter particle contribution to the

gamma-ray flux from the g.c. [8], but other hypotheses seem to work at least as well [9].

2. The dwarf spheroidal galaxies orbiting the Milky Way, like Segue-1, Ursa Minor, Draco, Sagittarius, Sculptor, Carina or Willman-1 [10–12]. The problem here is that the nature of many of these small, dark matter-dominated galaxies is not entirely clear, and the velocity dispersion estimates are based on rather small numbers of stars. Tidal disruption and confusion with star clusters are other complications. Thus the dark matter density profile is very uncertain for most of them. Nonetheless, by stacking the data together from many dwarf spheroidals these uncertainties can be made less severe, and preliminary results from Fermi-LAT shows this method to give quite promising results [13].

3. Galaxy clusters. This possibility has been less studied, however we noted in a previous Letter [14] that there are certain advantages that work in favour of this possible target for gamma-ray detection of dark matter annihilation. Galaxy clusters constitute the most massive objects in our Universe that are forming today. This causes their DM subhalo mass function to be less affected by tidal stripping compared to galaxy sized halos that formed long ago. The annihilation luminosities of the DM halo component for e.g. the Virgo cluster and the Draco dwarf scales in a way (see [14]) that the ratio of gamma-ray luminosities from the smooth components is around 4, in favour of Virgo. In addition, there may be a further enhancement due to substructure, which to a large extent should be unaffected by tidal disruption, at least in the outer regions. According to a recent estimate [15], more massive haloes tend to have a larger mass fraction in subhalos. For example, cluster size haloes typically have 7.5 per cent of the mass within  $r_{200}$  in substructures of fractional mass larger than  $10^{-5}$ , which is 25 per cent higher than galactic haloes [16].

For a satellite dwarf galaxy, however, once it is accreted by the Milky Way, the outer regions are severely affected by tidal stripping. The longer a satellite has been part of our Galaxy, and the closer it comes to the center during its pericentral passage, the more material is removed [17].

In this paper, we will investigate in some more detail the potential of several of the most promising galaxy clusters to yield an annihilation gamma-ray yield which

---

\* apinzke@physics.ucsb.edu

† pfrommer@cita.utoronto.ca

‡ lbe@fysik.su.se

could be observable with present and planned gamma-ray detectors.

For previous work related to dark matter in clusters, see, e.g., [18, 19].

**Anders, insert your flux table for various clusters, and discuss it**

This yields Fornax ( $M_{200} = 10^{14} M_{\odot}$ ) and Virgo ( $M_{200} = 2.1 \times 10^{14} M_{\odot}$ ) [] as the prime targets for DM observations, Perseus ( $M_{200} = 7.7 \times 10^{14} M_{\odot}$ ) for CR induced emission and we additionally decide in favor of the well studied cluster Coma ( $M_{200} = 1.4 \times 10^{15} M_{\odot}$ ) for comparison.

**(DELETED TEXT)**

## II. THEORY

### A. Astrophysics

The differential photon flux within a given solid angle  $\Delta\Omega$  along a line-of-sight (los) is given by

$$\frac{dF_{\gamma}}{dE_{\gamma}} \equiv \frac{d^3 N_{\gamma}}{dA dt dE_{\gamma}} = \frac{1}{2} \int_{\Delta\Omega} d\psi \sin \psi \frac{dS_{\gamma}}{dE_{\gamma}}(\psi, E_{\gamma}), \quad (1)$$

where

$$\frac{dS_{\gamma}}{dE_{\gamma}}(\psi, E_{\gamma}) = \int_{\Delta\Omega} d\Omega \int_{\text{los}} dl q_{\text{sum}}(E_{\gamma}, r) \Lambda(\theta), \quad (2)$$

and  $S_{\gamma}(\psi, > E_{\gamma})$  denotes the surface brightness above the photon energy  $E_{\gamma}$ . The integration along the line-of-sight  $l$ , in the direction  $\psi$  that the detector is pointing, is parameterized such that the radius of the source  $r = \sqrt{l^2 + D^2 - 2Dl \cos \Psi}$ , where  $D$  is the distance to the source from the galactic center and  $\cos \Psi \equiv \cos \theta \cos \psi - \cos \varphi \sin \theta \sin \psi$ . The angular integration  $d\Omega = \sin \theta d\theta d\varphi$  is performed over a cone centered around  $\psi$  and the opening angle  $\Delta\Omega$  is typically taken to be a few times the point spread function (PSF)  $\theta_{\text{res}}$ . The limited angular resolution results in a probability that a photon coming from a direction  $\psi'$  is instead reconstructed to a direction  $\psi$ , where the underlying probability distribution follow a Gaussian:

$$\Lambda(\theta) = \frac{1}{2\pi\theta_{\text{res}}^2} \exp\left[-\frac{\theta^2}{2\theta_{\text{res}}^2}\right], \quad \text{where } \theta = \psi' - \psi. \quad (3)$$

We denote the total differential source function by  $q_{\text{sum}}(E_{\gamma}, r)$ , where we include contributions from five main processes; leptophilic DM annihilating either indirectly through  $\mu^+/\mu^-$  to  $e^+/e^-$  or directly to  $e^+/e^-$  pairs that inverse Compton upscatter background photons (LP-IC), leptophilic DM emitting final state radiation (LP-FSR), supersymmetric DM benchmark models where annihilating neutralinos generate  $e^+/e^-$  pairs that upscatter background photons (BM-IC) and emit a continuum as well as final state radiation (BM-Cont), and

CR proton induced  $\pi^0$ :s decaying into gamma-rays (CR- $\pi^0$ ). The source function is given by

$$q_{\text{sum}}(E_{\gamma}, r) = q_{\text{CR}-\pi^0}(E_{\gamma}, r) + \sum_i q_{\text{sm},i}(E_{\gamma}, r) B_{\text{tot},i}(\sigma_v, r) \quad (4)$$

the differential CR to gamma-ray source function is denoted by  $q_{\text{CR}-\pi^0}(E_{\gamma}, r)$  (see Sect. II A 2 and [20] for further details). The subscript  $i$  runs over the gamma-ray producing DM channels and the total differential boost factor for DM is given by  $B_{\text{tot},i}(r, \sigma_v) = B_{\text{sfe}}(\sigma_v) B_{\text{sub},i}(r)$ . It is the product of enhancement factors from SFE  $B_{\text{sfe}}(\sigma_v)$  (see Sect. II B 1) and from substructure enhancement over the smooth halo contribution  $B_{\text{sub},i}(r) = 1 + q_{\text{sub}}(r)/q_{\text{sm},i}(r)$  (see Sect. II A 1). The DM source function from the smooth halo for each process is written on the form:

$$q_{\text{sm},i}(E_{\gamma}, r) = \sum_j \frac{dN_{\gamma,j}}{dE_{\gamma}} \Gamma_j(r), \quad (5)$$

where the annihilation rate density is given by

$$\Gamma_j(r) = \frac{1}{2} \left[ \frac{\rho(r)}{m_{\chi}} \right]^2 \langle \sigma v \rangle_j. \quad (6)$$

Here the subscript  $j$  runs over all kinematically allowed gamma-ray producing channels each with the spectrum  $\frac{dN_{\gamma,j}}{dE_{\gamma}}$  and annihilation cross-section  $\langle \sigma v \rangle_j$ . We denote the DM mass with  $m_{\chi}$  and the DM density profile with  $\rho(r)$ . Typically the universal Navarro-Frenk-White (NFW) density profile provide a good fit to both the observed and simulated clusters. It can be considered as a special case of the more general 5-parameter profile:

$$\rho(r) = \frac{\rho_s}{(r/r_s)^{\gamma} [1 + (r/r_s)^{\alpha}]^{\delta}}, \quad \delta = \frac{\beta - \gamma}{\alpha}, \quad (7)$$

where a cuspy NFW profile is given by  $(\alpha, \beta, \gamma) = (1, 3, 1)$ . The scaling radius is given by  $r_s$  and the characteristic overdensity by

$$\rho_s(c) = \frac{\Delta \rho_c}{3} \frac{c^3}{\log(1+c) - c/(1+c)}, \quad (8)$$

where the halo mass dependent concentration parameter  $c$  is derived from a power-law fit to cosmological simulations with  $M_{200} \gtrsim 10^{10} M_{\odot}$  [21],

$$c = 3.56 \times \left( \frac{M_{200}}{10^{15} M_{\odot}} \right)^{-0.098}. \quad (9)$$

This mass scaling agrees well with [22] for cluster-mass halos after converting the concentration definitions according to [23]. In this work we choose to model the DM density by an Einasto density profile

$$\rho_{\text{ein}}(r) = \rho_{-2} \exp \left\{ -\frac{2}{\alpha} \left[ \left( \frac{r}{r_{-2}} \right)^{\alpha} - 1 \right] \right\}, \quad \alpha = 0.17, \quad (10)$$

that is slightly shallower in the center than the conventional Navarro-Frenk-White (NFW) profile, but provide a better fit to recent simulated high resolution DM halos [24]. It should also be noted that recent detailed galaxy cluster observations find a core like density profile with an inner slope of  $\beta = 0.6$ , where  $\beta \gtrsim 1$  can be ruled out to a  $> 95\%$  confidence [25]. In Eq. (10) we denote the density where the profile has a slope of  $-2$  by  $\rho_{-2}$ , and the radius by  $r_{-2}$ . Assuming that all the flux from an NFW profile originate from within the scale radius  $r_s = r_{200}/c$ , and all the flux from an Einasto profile originate within  $r_{-2} = r_{200}/c$ , it follows that  $\rho_{-2} = \rho_s/4$ .

### 1. Substructures

High-resolution DM only simulations of Milky Way (MW) type halos find substantial amount of substructures in the periphery of DM halos, while the substructures in the center are erased due to dynamical disruption. Since the rate of which DM is annihilating depends on the density squared, the resulting flux from substructures is boosted compared to the smooth density distribution. Recent high resolution simulations suggest a flux enhancement from substructures of the order of ten up to a few 100 [26, 27] for a MW size halo. We use a double power-law function to fit [28] the luminosity from the smooth component of substructures (i.e. substructures within substructures are not included) inside radius  $r$  which is determined for the Aquarius simulations [26, 29]. Our best fit is given by

$$L_{\text{sub}}(< r) = 0.76 C_1 C_2(M_{200}) L_{200\text{sm}} x^{0.95x^{-0.27}}, \quad (11)$$

where  $L_{200\text{sm}}$  is the luminosity from the smooth halo without substructures within  $r_{200}$  and  $x = \left(\frac{r}{r_{200}}\right)$ . The first normalization constant is derived from the simulations:

$$C_1 = \left(\frac{M_{\text{res, sim}}}{M_{\text{lim}}}\right)^{0.226}, \quad (12)$$

where  $M_{\text{res, sim}} = 10^5 M_\odot$  is the mass of the smallest resolved subhalos in the MW simulation, and  $M_{\text{lim}}$  is the theoretical smallest mass of subhalos determined from free streaming length of DM (CHECK). Here we assume that the power-law scaling relation in Eq. (12) is valid down to the free streaming mass of DM halos, which is conventionally in the cold dark matter universe [30, 31] taken to be  $10^{-6} M_\odot$ . Note that potentially the power-law could flatten towards smaller mass scales although current simulations show no hits of such a behavior and in addition we are approaching the asymptotic behavior in the power spectrum on these scales (CHECK). For DM halos more (less) massive than the MW we expect a larger (smaller) boost from substructures, simply because of the larger (smaller) mass range down to the minimum

mass  $M_{\text{lim}}$ . We capture this halo mass dependence with the second normalization in Eq. (11):

$$C_2(M_{200}) = \left(\frac{M_{200}}{M_{200\text{sim}}}\right)^{0.226}, \quad (13)$$

where  $M_{200\text{sim}} = 1.9 \times 10^{12} M_\odot$  is the mass of the MW halo in the simulation [29].

The different density profiles have a large impact on the luminosity from annihilating DM, although the details of the density profile can be neglected compared to the dominating boost from substructures. In Fig. 1 we compare the radial dependence of the accumulative luminosity from different smooth cluster density profiles to the substructure boosted luminosity at different mass scales. We recalculate the density contrast for the core like NFW density profile  $\rho_s$  and rescale the concentration parameter in Eq. (9) with 300/160 [25] to account for the more centralized scale radius in cluster with a softer cusp. The emission coming from the core like NFW density profile ( $\beta = 0.6$ ) compared to a cuspy ( $\beta = 1.0$ ) is about 30% larger within  $r_{200}$ . This difference is build up within 10% of  $r_{200}$  (i.e. close to  $r_s$ ). Hence the slope of the central part of a cluster is unimportant for the DM luminosity inside  $r_{200}$ , instead the important factor is the scale radius. The emission from an Einasto density profile is about 50% larger than the cuspy NFW profile in the periphery of the cluster, where the difference is mainly build up at a few percent of  $r_{200}$ . The substructure boosted luminosities is negligible in the center of halos, but integrated out to  $r_{200}$  the boost is about; 10 for dwarf galaxies,  $10^2$  for galaxies, and  $10^3$  for galaxy clusters.

In Fig. 2 we show the radius with the maximum luminosity for substructures and smooth density profiles, both for three different mass scales. We find that the smooth luminosity per logarithmic radial bin peaks at  $xd^2L/dx^2 + dL/dx = 0 \rightarrow r \propto r_{200}/3c$ . Hence the main contribution to the luminosity for large mass scales, which are usually associated with a low concentrated DM halos, is focused to the regime around 10% of  $r_{200}$ . It clearly shows how that the main contribution from the substructures is coming from outer parts of the DM halos, while the main contribution from the smooth density profiles peaks around the scale radius. Not that, even though the bulk of substructures have been erased in the central regions of DM halos, a cluster in projection has a significant enhancement due to substructures at a radius of just a few percent of  $r_{200}$ .

### 2. Cosmic-ray induced gamma-ray emission

On small astrophysical scales, such as supernovae remnants and galaxies, there are convincing evidences of non-thermal populations. Especially, in the MW, the cosmic rays are observed directly as well as indirectly through radio, X-ray, and gamma-ray emission. On larger scales

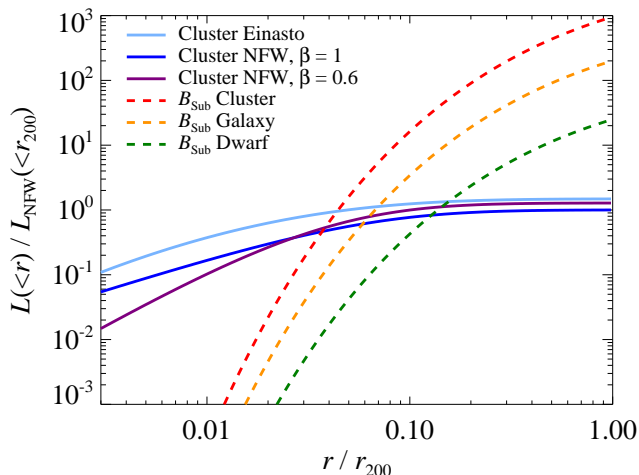


FIG. 1. Radial dependence of various luminosity contributions. The solid lines show the accumulative smooth luminosity from a cluster with the mass  $M_{200} = 10^{15} M_{\odot}$  for three different density profiles; an Einasto profile with  $\alpha = 0.17$  (light blue), a cuspy NFW profile with  $\beta = 1.0$  (dark blue), and a core NFW profile with  $\beta = 0.6$  (purple). The dashed lines show the accumulative luminosity from substructures for three different mass scales; an  $M_{200} = 10^{15} M_{\odot}$  galaxy cluster (red), an  $M_{200} = 10^{12} M_{\odot}$  galaxy (orange), and an  $M_{200} = 10^8 M_{\odot}$  dwarf galaxy (green). All luminosities have been normalized with the luminosity within  $r_{200}$  from a cuspy NFW profile. We have assumed the standard value for the limiting substructure mass of  $M_{\text{lim}} = 10^{-6} M_{\odot}$ . Note the large expected boost from substructures in clusters ( $\sim 1000$ ), and the relative small boost in dwarf galaxies ( $\sim 20$ ).

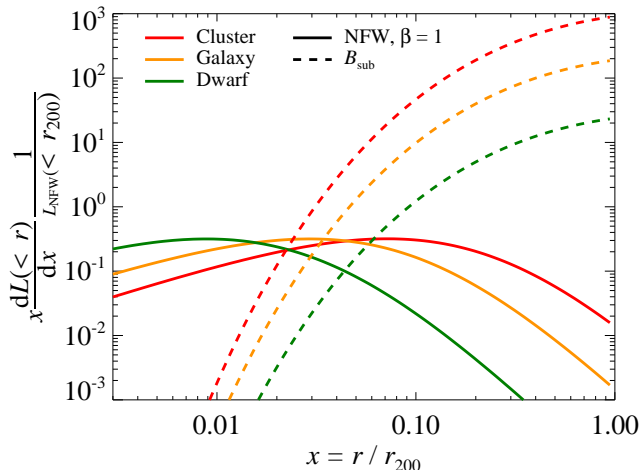


FIG. 2. Luminosity dominated radius for different mass scales. The solid lines show the emissivity from a cuspy  $\beta = 1.0$  NFW density profile for three different mass scales; an  $M_{200} = 10^{15} M_{\odot}$  galaxy cluster (red), an  $M_{200} = 10^{12} M_{\odot}$  galaxy (orange), and an  $M_{200} = 10^8 M_{\odot}$  dwarf galaxy (green). The dashed lines show the emissivity from substructures for the same three mass scales. All emissivities have been normalized with the luminosity within  $r_{200}$  from a cuspy NFW profile. We have assumed the standard value for the limiting substructure mass of  $M_{\text{lim}} = 10^{-6} M_{\odot}$ .

of the order of few 100 kpc up to Mpc, there are currently a vast number of observations of radio emission coming from radio mini halos in the center of cooling flow clusters, radio relics in the periphery of clusters [32] as well as smooth giant radio halos that have been observed in more than 50 clusters [33, 34]. This type of emission is expected in clusters since the formation process of a galaxy cluster is a very energetic processes that induces both turbulence as well as frequently occurring merging and accretion shocks which both are thought to accelerate large quantities of relativistic non-thermal protons and radio emitting electrons to high energies. Thus most of the observed radio emission in clusters is expected to emerge from cosmic-ray electron induced radio synchrotron emission. The precise origin of these electrons, in especially relics and giant radio halos, is still not settled. However, due to the smoothness of the extended emission and the observed power-law slope it seems quite natural that they are of hadronic origin. Especially since the long cooling time of cosmic ray protons (CRps) allows for both an extended and large population of CRps to build up over the cluster history [35].

When the CRps interact with ambient gas protons, it results in the production of both charged and neutral pions that decay into electrons, neutrinos, and gamma-rays. The production of these secondaries depend both on the gas and CRp densities in the cluster, where the CRp density roughly trace the gas outside the core regime and is slightly enhanced in the center. This density scaling implies that clusters are great targets for Cherenkov telescopes with a high sensitivity for the central parts of close by clusters. Detecting the cluster gamma-ray emission is crucial in this respect as it potentially provides the unique and unambiguous evidence of CRp populations in clusters through observing the  $\pi^0$  bump at about 100 MeV in the spectra.

We adopt the spectrally and spatially universal gamma-ray model developed by Pinzke & Pfrommer [20] to estimate the emission from decaying  $\pi^0$ s that dominates over the inverse Compton emission from primary and secondary electrons above 100 MeV in clusters. The gamma-ray formalism was derived from high resolution simulations of clusters of galaxies that included radiative hydrodynamics, star formation, supernova feedback, and followed CRp physics using a novel formulation that trace the most important injection and loss processes self-consistently while accounting for the CRp pressure in the equation of motion [36–38]. We note that the overall normalization of the CRp and gamma-ray distribution scales with the maximum acceleration efficiency at structure formation shock waves. Following recent observations at supernova remnants [39] as well as theoretical studies [40], we adopt a realistic value of this parameter and assume that 50% of the dissipated energy at strong shocks is injected into CRps while this efficiency rapidly decreases for weaker shocks [37].



## B. Particle physics

### 1. Leptophilic models

Sommerfeld enhancement, electron spectra

### 2. Supersymmetric dark matter

neutralino, benchmark models, continuum emission, electron spectra

### 3. Final state radiation

The photon spectrum from resulting from FSR is universal with only a weak dependence of the underlying particle physics model. The photon yield from this process is given by (see e.g. [41])

$$\frac{dN_{X\bar{X}}}{dx} \approx \frac{\alpha Q_X^2}{\pi} \mathcal{F}_X(x) \log \left[ \frac{4m_X^2(1-x)}{m_X^2} \right]. \quad (14)$$

Here, the normalized photon energy  $x = E_\gamma/m_X c^2$ ,  $\alpha = e^2/\hbar c$  is the fine-structure constant,  $Q_X^2$  and  $m_X$  the charge and mass of the particle  $X$ , respectively. The function  $\mathcal{F}_X(x)$  depends on the spin of the final state and is given by

$$\mathcal{F}_{\text{fermion}}(x) = \frac{1 + (1-x)^2}{x} \quad (15)$$

for fermions.

## C. Radiative processes

In this section we outline the basics of inverse Compton (IC) emission. As target radiation fields we consider both cosmic microwave background (CMB) photons, and the light from stars and dust (SD). We derive a semi-analytic model from which we can estimate the spectral and spatial distributions of SD as a simple function of cluster mass.

### 1. Inverse Compton

The standard IC source function is given by [42]:

$$q_{\text{IC}}(E_\gamma, r) = \frac{d^3 N_\gamma}{dV dt dE_\gamma} = \frac{3}{4} c \sigma_T \int dE_{\text{ph}} \frac{n_{\text{ph}}(E_{\text{ph}})}{E_{\text{ph}}} \times \int dE_e \frac{dn_e}{dE_e}(E_e, r) \frac{(m_e c^2)^2}{E_e^2} G(\Gamma_e, q), \quad (16)$$

where  $E_e$  is the energy of the upscattering electrons and  $E_{\text{ph}}$  is the energy of the background photon field. We

represent the Thomson cross-section with  $\sigma_T$  and the full differential Klein-Nishina (KN) cross-section is captured by [43]:

$$G(\Gamma_e, q) = 2q \ln q + (1 + 2q)(1 - q) + \frac{1}{2} \frac{(\Gamma_e q)^2 (1 - q)}{1 + \Gamma_e q}, \quad (17)$$

where

$$\Gamma_e = \frac{4E_{\text{ph}} E_e}{(m_e c^2)^2}, \quad \text{and} \quad q = \frac{E_\gamma}{\Gamma_e (E_e - E_\gamma)}. \quad (18)$$

The full KN cross-section accounts for the less efficient energy transfer between the photon and electron and results in a steepening of the IC gamma-ray spectrum. In the low energy Thomson regime the IC spectrum  $F_\gamma \sim E_\gamma^{-(\alpha_e - 1)/2}$ , however when  $\Gamma_e \gg 1$  the IC spectrum steepens due to the KN suppression to  $E_\gamma^{-\alpha_e} \log(E_\gamma)$ . Here we denote the steady state electron spectrum by  $\alpha_e$ .

We account for two major contributions to the number density of radiative background fields  $n_{\text{ph}}$ ; the CMB photons and the infra-red (IR) to ultra-violet (UV) light emitted by SD. The number density for the SD is given by  $n_{\text{ph}} \equiv \frac{d^2 N_{\text{ph}}}{dV dE_{\text{ph}}}(E_{\text{ph}}, r) = \frac{u_{\text{SD}}(E_{\text{ph}}, r)}{E_{\text{ph}}^2}$  where the SD energy density  $u_{\text{SD}}(E_{\text{ph}}, r)$  is given in Eq. (38). We model the CMB photon spectrum as a photon gas that is isotropically distributed and follows a black body spectrum with the temperature  $T = 2.73$  K:

$$n_{\text{ph}}(E_{\text{ph}}) = \frac{d^2 N_{\text{ph}}}{dV dE_{\text{ph}}} = \frac{1}{\pi^2 (\hbar c)^3} \frac{E_{\text{ph}}^2}{\exp(E_{\text{ph}}/k_B T) - 1}. \quad (19)$$

Note that the typical energy of a black body photon before scattering is given by  $\langle E_{\text{ph}} \rangle = \epsilon_{\text{ph}}/\tilde{n}_{\text{ph}} \approx 2.70 k_B T$ , where  $\tilde{n}_{\text{ph}}$  and  $\epsilon_{\text{ph}}$  are the number- and energy-density derived by integrating  $n_{\text{ph}}(E_{\text{ph}})$  and  $E_{\text{ph}} n_{\text{ph}}(E_{\text{ph}})$  over the photon energy  $E_{\text{ph}}$ , respectively.

The electrons injected from annihilating DM also suffer from diffusive and radiative losses. Hence we have to calculate the equilibrium spectrum of the electrons plus positrons denoted by  $\frac{dn_e}{dE_e}$  in Eq. (16). We derive this stationary solution using the CR transport equation (neglecting convection and re-acceleration effects):

$$\frac{\partial}{\partial t} \left( \frac{dn_e}{dE_e} \right) = \nabla \left[ D(E_e, \mathbf{x}) \nabla \frac{dn_e}{dE_e} \right] + \frac{\partial}{\partial E_e} \left[ b(E_e, \mathbf{x}) \frac{dn_e}{dE_e} \right] + q_e(E_e, \mathbf{x}), \quad (20)$$

where  $D(E_e, \mathbf{x})$  denotes the diffusion coefficient and  $b(E_e, \mathbf{x})$  the energy loss term. The source function  $q_e(E_e, \mathbf{x})$  yields the number of electrons and positrons produced per unit time, energy and volume element at the position  $\mathbf{x}$ :

$$q_e(E_e, r) = \sum_f \frac{dN_{e,f}}{dE_e}(E_e) B_f \Gamma_f(r), \quad (21)$$

where the annihilation rate density  $\Gamma_f(r)$  is defined in Eq. (6). The sum runs over the kinematically allowed annihilation final states  $f$ , each with a branching ratio  $B_f$  and a differential spectrum  $\frac{dN_e^f}{dE_e}$  that represents the number of electrons plus positrons resulting from an annihilation event. For neutralinos annihilating directly into electrons and positrons we model the spectral distribution with  $\frac{dN_e^f}{dE_e} = 2\delta(E_e - m_\chi c^2)$ . We use DarkSUSY to compute both the spectra when neutralinos annihilate directly into a  $\mu^+$  and  $\mu^-$  in the leptophilic model as well as in the four BM models where a fraction of the annihilating neutralinos is converted into electrons and positrons (see Sect. II B and Fig. 18 for further details).

The electrons and positrons lose their energy on a timescale that is shorter than the diffusive timescale in the ICM of galaxy clusters for CR electrons with  $E_e \gtrsim \text{MeV}$  (CHECK). Hence, we neglect the first term of the r.h.s. in Eq. (20), and derive an expression for the equilibrium number density:

$$\frac{dn_e}{dE_e}(E_e, r) = \frac{1}{b(E_e, r)} \int_{E_e}^{m_\chi c^2} dE'_e Q(E'_e, r), \quad (22)$$

$$b(E_e, r) = \tilde{b} \left[ \frac{B_{\text{CMB}}^2}{8\pi} + \frac{B^2(r)}{8\pi} + u_{\text{SD}}(r) \right] E_e^2, \quad (23)$$

$$\tilde{b} = \frac{4\sigma_{\text{TC}}}{3(m_e c^2)^2}. \quad (24)$$

Here we include the three main radiative loss processes for the CR electrons and positrons: (1) IC losses on CMB photons where the equivalent field strength of the CMB is denoted by  $B_{\text{CMB}} = 3.24\mu\text{G}$ . (2) Synchrotron losses on ambient magnetic fields where we parameterize the magnetic field in the galaxy cluster by  $B(r) = 3\mu\text{G} [n_e(r)/n_e(0)]^{\alpha_B}$ , which follows from flux frozen magnetic fields. We adopt a magnetic decline of  $\alpha_B = 0.7$  in this work. (3) IC losses on starlight and dust with an energy density  $u_{\text{SD}}(r)$  given by Eq. (38), which we derive in the following subsection.

#### IC – dust and starlight

Galaxy clusters are typically characterized by the hot gas in the ICM and the collection of gravitationally bound galaxies. The emission in the IR and UV wavelengths emerge from dust and starlight in both the galaxies and the ICM (e.g. [44] and [45]). Much of the radiation leaks out from the galaxy into the ICM, which give rise to similar spectral distributions for the galaxies and the ICM in these wavelengths. Hence, we use the accurately measured light from galactic dust and starlight for the ISM to model the ICM. We characterize the spectra through a fit to the galactic spectra presented in [44]. The spatial distribution of the SD light in clusters is extracted from a stacked emission analysis of Sloan Digital Sky Survey (SDSS) data at the redshift  $\sim 0.25$  [46]. Finally, we fix the normalization for the light from stars and dust in an galaxy cluster individually using the IR to X-ray luminosity scaling relation found in [47]. The X-ray luminosities for the clusters used in this work are listed in the extended HIGHEST X-ray FLUX Galaxy Cluster Sample

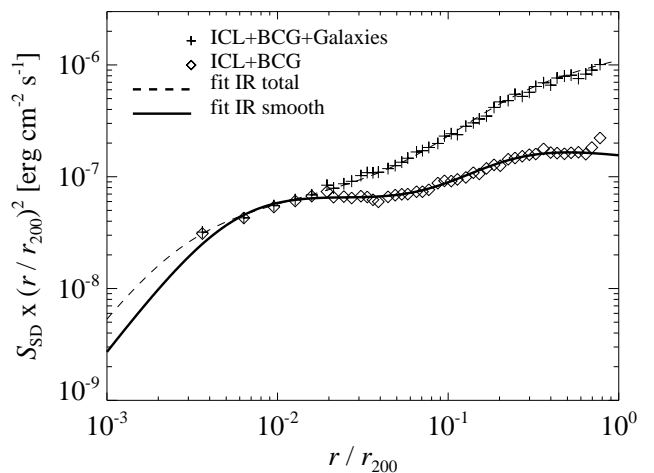


FIG. 3. *Spatial dependence of light from stars and dust.* We show 2D surface brightness profiles in the  $r$ -band ( $\sim 1\text{eV}$ ) obtained from stacked clusters in the Sloan Digital Sky Survey (SDSS) at the redshift  $z \sim 0.25$  [46]. The brightness profiles have been weighted with the  $r_{200}$  normalized area inside radius  $r$ , and trace the radial dependence of the luminosity from stars and galaxies. The crosses show the total observed starlight including the diffuse intracluster (ICL), the galaxies, and the brightest cluster galaxy (BCG) in the center of the cluster. The diamonds denote the observed starlight from the ICL and the BCG. The solid line show the fit to the data of the total light including the ICL, the BCG, and the galaxies, while the dashed line that is fitted to only the ICL and the BCG.

(HIFLUGCS) [48] from the Rosat all-sky survey. Note that we have added the Virgo cluster to the sample that we nevertheless refer to as extended HIFLUGCS catalogue in the following.

#### Spatial distribution – stars and dust

Our goal in this section is to derive a simple spatial model for the distribution of SD in galaxy clusters. For this reason we use stacked cluster observations by Sloan in the  $r$ -band that trace the stars. We assume that the dust trace the stars in the clusters, which should be accurate to the order of magnitude estimate that we are interested in here. The stacked surface brightness profiles in [46] are measured at redshift  $z \sim 0.25$  with an average mass of the clusters of  $4.0 \times 10^{13} M_\odot$ . The profiles are build up out of three components; diffuse intracluster light (ICL), galaxies, and the brightest cluster galaxy (BCG) in the center of clusters. However, the total volume overlap of the ISM to the cluster is very small compared to the ICL- and BCG overlap with the cluster, thus the relative contribution of the galaxies to the IC emission is suppressed. To remove this bias we cut out the galaxies that have been smoothed over the cluster in the stacked analysis. In Fig. 3 we show the SDSS stacked brightness profiles as well as the fitted profiles [49]. Our benchmark spatial model are show with the solid black line, and include the contribution from the ICL and BCG.

Instead of modelling the surface brightness with a de Vaucouleur profile with the addition of a power-law, we use a double beta profile model for simplicity of deprojection given by:

$$S_{\text{SD}}(r_{\perp}) = \sum_{i=1}^2 S_i \left[ 1 + \left( \frac{r_{\perp}}{r_{c_i}} \right)^2 \right]^{-3\beta_i + 1/2}, \quad (25)$$

where we found the following best fitted central brightness ( $S_i$ ), core radius ( $r_{c_i}$ ), and slope ( $\beta_i$ ):

$$\begin{aligned} S_1 &= 1.4 \times 10^{-5} \text{ erg cm}^{-2} \text{ s}^{-1}, \quad r_{c_1} = 210 \text{ kpc}, \quad \beta_1 = 0.44 \\ S_2 &= 6.0 \times 10^{-3} \text{ erg cm}^{-2} \text{ s}^{-1}, \quad r_{c_2} = 2.8 \text{ kpc}, \quad \beta_2 = 0.45. \end{aligned} \quad (26)$$

The 3D spatial profile is derived by deprojecting the surface brightness in Eq. (25) (see e.g. [50] for details about the deprojection):

$$j(r) = \sum_{i=1}^2 \frac{S_i}{2\pi r_{c_i}} \frac{6\beta_i - 1}{(1 + r^2/r_{c_i}^2)^{3\beta_i}} \mathcal{B}\left(\frac{1}{2}, 3\beta_i\right), \quad (27)$$

where  $\mathcal{B}(a, b)$  denotes the beta-function [51].

#### Spectral distribution – stars and dust

Our goal in this section is to derive a simple spectral model for SD in galaxy clusters. Since the radiation from galaxies are expected to leak out into the ICM, we expect similar spectral distributions, at least to the order of magnitude that we are interested in here. Hence, we use the IR to UV spectrum derived in [44] for a MW type galaxy to characterize the spectral distribution of light from SD in a cluster. Note, however, that we only keep the spectral shape, and renormalize the spectral distribution using the luminosity from SD.

In Fig. 4 we show the spectral distribution of the light from SD together with the CMB black-body distribution in a galaxy cluster, both at the radius  $r = 0.071r_{200}$  where the smooth energy density of the SD light (see Fig. 5) equals the energy density of the CMB. We have renormalized both the spectral data and the fitted spectra using the luminosity from stars and dust individually (see below for further details about the renormalization). We choose to fit the spectrum of the dust that peaks at about  $10^{-2}$  eV with a double power-law, and the slightly wider spectral distribution of the stars that peaks at about 1 eV with a tripple power-law. We find

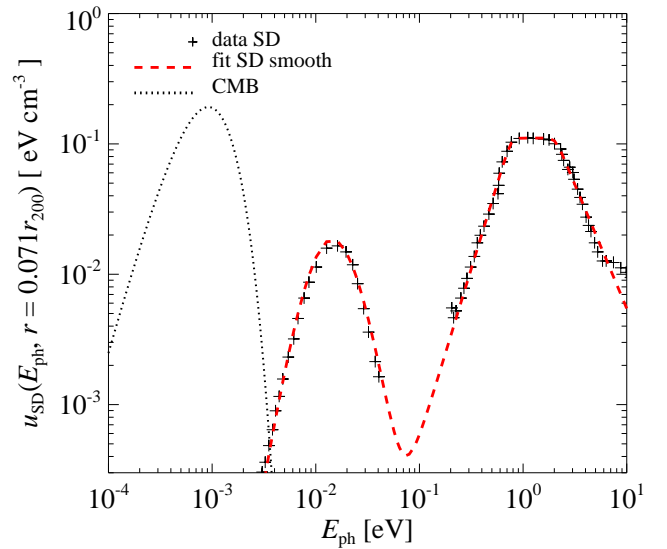


FIG. 4. Spectral dependence of radiation fields in a cluster of galaxies. The black dotted line in the left peak show the spectrum of CMB photons using a black body with a temperature of 2.73 K. The crosses in the middle and right peaks represent the measured spectra from stars and dust (SD), respectively, and are derived in [44] for a galaxy. We normalize the individual SD spectrum separately using the observed luminosity from SD in clusters. The SD luminosity is related to the cluster mass through Eq. where we use have used the mass  $M_{200} = 4.0 \times 10^{13} M_{\odot}$  in this figure. Finally we renormalize the SD spectra to the radius  $r = 0.071r_{200}$ , where the smooth energy density of the SD light (see Fig. 5) equals the energy density of the CMB. The red dashed lines show the fitted SD spectral model.

the best fit spectra for the SD in a cluster through:

$$E_{\text{ph}}^2 \frac{d^2 N_{\text{ph}}}{dE_{\text{ph}} dV} \equiv u_{\text{SD}}(E_{\text{ph}}) = \sum_i N_i(L_X) u_i^{\text{gal}}(E_{\text{ph}}), \quad (28)$$

where  $i = \{\text{stars, dust}\}$  and

$$\begin{aligned} u_{\text{stars}}^{\text{gal}}(E_{\text{ph}}) &= \frac{23 \text{ eV}}{\text{cm}^3} \left( \frac{1.23 \text{ eV}}{E_{\text{ph}}} \right)^{1.9} \\ &\times \left[ 1 + \left( \frac{2.04 \text{ eV}}{E_{\text{ph}}} \right)^{20} \right]^{-\frac{1.9}{20}} \\ &\times \left[ 1 + \left( \frac{0.78 \text{ eV}}{E_{\text{ph}}} \right)^{20} \right]^{-\frac{2.6}{20}}, \end{aligned} \quad (29)$$

$$\begin{aligned} u_{\text{dust}}^{\text{gal}}(E_{\text{ph}}) &= \frac{40 \text{ eV}}{\text{cm}^3} \left( \frac{0.0144 \text{ eV}}{E_{\text{ph}}} \right)^{4.9} \\ &\times \left[ 1 + \left( \frac{0.0144 \text{ eV}}{E_{\text{ph}}} \right)^{1.9} \right]^{-4.9}. \end{aligned} \quad (30)$$

#### Normalization

**HARD TO READ FIRST PART** The spatial and spectral distribution functions of the light from SD in a cluster are both normalized with a constant determined from

the luminosity in each respective wavelength. The specific energy density is given by

$$\begin{aligned} u_{\text{SD}}(E_{\text{ph}}, r) &= \frac{j(r)}{j(0)} u_{\text{SD}}(E_{\text{ph}}) \\ &= \frac{j(r)}{j(0)} \sum_i N_i(L_X) u_i^{\text{gal}}(E_{\text{ph}}), \end{aligned} \quad (31)$$

where we fix the unitless normalization  $N_i(L_X)$  using the total energy of the light in SD ( $E_{i,\text{vir}}$ ) within  $r_{200}$ :

$$\begin{aligned} E_{i,\text{vir}} &= L_i \frac{r_{200}}{c} \\ &= N_i(L_X) \int_{r_{200}} \int_i \frac{j(r)}{j(0)} \frac{u_i^{\text{gal}}(E_{\text{ph}})}{E_{\text{ph}}} dV dE_{\text{ph}}, \end{aligned}$$

for  $i = \{\text{stars}, \text{dust}\}$ . (32)

Here we approximate the total energy of the photons within  $r_{200}$  with the luminosity  $L_i$  [47] times the typical timescale it takes for a photon to propagate through the cluster (we assume that the cluster is optically thin). Once we derived the SD luminosities for a well representative cluster, we use a IR to X-ray scaling relation to estimate the luminosity from an arbitrary cluster:

$$L_{\text{ir}} = 1.05 \times 10^{45} \text{ erg s}^{-1} \left( \frac{L_X}{10^{44} \text{ erg s}^{-1}} \right)^{0.53}, \quad (33)$$

where  $L_X$  is the luminosity of the X-ray emitting gas within  $r_{200}$ .

The normalization constant for the starlight  $N_{\text{stars}}(L_X)$  is derived in the following three steps: (1) We use the average apparent magnitude in the  $(r+i)$ -band  $m_{(r+i),0.25} \approx 15.5$  [46] of a cluster with the average mass  $M_{200} = 4.0 \times 10^{13} M_{\odot}$  at a redshift  $z = 0.25$  to derive the luminosity from the stars:

$$L_{\text{stars}} = 10^{\frac{m_{\odot} - m_{(r+i),0.25}}{2.5}} \left( \frac{D_{\text{cl}}}{D_{\odot}} \right)^2 L_{\odot} \approx 7.1 \times 10^{44} \text{ erg s}^{-1}, \quad (34)$$

where the apparent magnitude of the sun  $m_{\odot} \approx -27.1$ , the distance to the sun  $D_{\odot} = 4.85 \times 10^{-6} \text{ pc}$ , the luminosity of the sun  $L_{\odot} = 3.85 \times 10^{34} \text{ erg s}^{-1}$ , and the distance to the cluster  $D_{\text{cl}} = 1.26 \times 10^9 \text{ pc}$ . (2) We use the IR to X-ray scaling relation in Eq. (33) to derive a more general form of the luminosity from stars in Eq. (34) that is valid for an arbitrary cluster mass. The cluster X-ray luminosities are found in the extended HIFLUGCS catalogue [48] to which we have added the Virgo cluster. (3) The normalization constant for the stars is determined from the above steps together with Eq. (32) where we integrate over the cluster volume and spectral distribution of the stars. It is given by

$$N_{\text{stars}}(L_X) = 1.2 \times 10^{-9} \left( \frac{L_X}{10^{44} \text{ erg s}^{-1}} \right)^{0.53}. \quad (35)$$

Note that since the luminosities include the contribution from galaxies, we have integrated the spatial distribution

including galaxies to derive the normalization. Once the normalization is fixed, the SD energy densities are derived from the spatial distribution where galaxies have been excluded.

The normalization constant for the dust  $N_{\text{dust}}(L_X)$  is derived in the following four steps: (1) We use a cluster with the the average mass  $M_{200} = 4.0 \times 10^{13} M_{\odot}$  and estimate the X-ray luminosity from the X-ray to mass scaling relations derived for the Representative XMM-Newton Cluster Structure Survey (REXCESS) in [52]:

$$L_X = 1.18 \times 10^{44} \text{ erg s}^{-1} \left( \frac{M_{200}}{10^{14} M_{\odot}} \right)^{1.81}, \quad (36)$$

where we have used that  $M_{200} \approx 1.58 M_{500}$  for a small cluster [53]. (2) From the IR to X-ray scaling relation in Eq. (33) we can now estimate calculate the luminosity from the dust for a  $M_{200} = 4.0 \times 10^{13} M_{\odot}$  cluster;  $L_{\text{dust}} = 4.7 \times 10^{44} \text{ erg s}^{-1}$ . (3) We generalize Eq. (34) to an arbitrary cluster mass using Eq. (33) together with the cluster X-ray luminosities in the extended HIFLUGCS catalogue. (4) The normalization constant for the dust can now be determined from the above steps together with Eq. (32) where we integrate over the cluster volume and spectral distribution of the dust. It is given by

$$N_{\text{dust}}(L_X) = 1.4 \times 10^{-9} \left( \frac{L_X}{10^{44} \text{ erg s}^{-1}} \right)^{0.53}. \quad (37)$$

Note that since the luminosities include the contribution from galaxies, we have integrated the spatial distribution including galaxies to derive the normalization. Once the normalization is fixed, the SD energy densities are derived from the spatial distribution where galaxies have been excluded.

#### Energy density

The spatial distribution of the SD energy density is an important quantity since it impacts the steady state electron and positron spectra through cooling. A higher density of SD in a cluster suppresses the spectra of the upscattering particles. With the formalism presented above, we can now derive the energy density from starlight and dust in a galaxy cluster through

$$\begin{aligned} u_{\text{SD}}(r) &= \int dE_{\text{ph}} \frac{d^2 N_{\text{ph}}}{dE_{\text{ph}} dV} E_{\text{ph}} = \int dE_{\text{ph}} \frac{u_{\text{SD}}(E_{\text{ph}}, r)}{E_{\text{ph}}} \\ &= \frac{j(r)}{j(0)} \int dE_{\text{ph}} \sum_i N_i(L_X) u_i^{\text{gal}}(E_{\text{ph}}). \end{aligned} \quad (38)$$

In Fig. 5 we compare the energy densities from different radiation fields in a galaxy cluster with the mass  $M_{200} = 4.0 \times 10^{13} M_{\odot}$ . We use two different profiles for the SD energy density, where the total profile includes the contribution from the ICL, the BCG and all the galaxies, while the galaxies are excluded in the smooth profile. We find that even for a cluster with a relative small mass



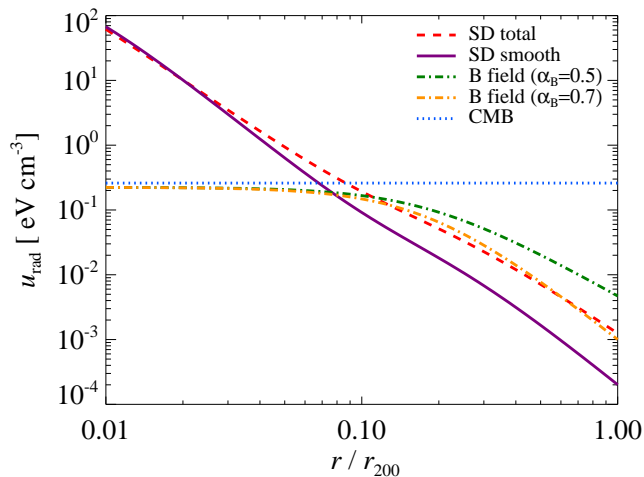


FIG. 5. Spatial dependence of the energy density of radiation fields in a cluster of galaxies. The energy density of the CMB, shown by the blue dotted line, is isotropic throughout the cluster, hence represented by a flat profile with  $u_{\text{cmb}} = 0.26 \text{ eV cm}^{-3}$ . The energy density of the light from stars and dust (SD) is denoted by the red dashed line and the solid purple line for the total SD light and the smooth SD light, respectively. The SD light has been renormalized to a cluster with the mass  $M_{200} = 4.0 \times 10^{13} M_{\odot}$ . Finally we show the energy density two magnetic field models with a central magnetic field of  $3 \mu\text{G}$ . The magnetic field scales with the gas density to the power  $\alpha_B$ ; green dash-dotted line ( $\alpha_B = 0.5$ ) and orange dash-dotted line ( $\alpha_B = 0.7$ ). Note that the SD radiation is dominating the energy density inside  $\sim 0.1 r_{200}$ .

the energy density of the SD components dominates over the CMB and the magnetic fields (with a central B field of  $3 \mu\text{G}$ ) within about 10% of  $r_{200}$ . Outside this radius the CMB is dominating the energy density of the cluster, hence the magnetic fields are always subdominant in the cluster and can safely be removed from cluster IC calculations for a reasonable central density and spectral index. Although, in this work we keep the contribution from B-fields to the total energy density for consistency.

(DELETED TEXT)

### III. SPECTRAL GAMMA-RAY DISTRIBUTION

Spectrally resolved indirect DM searches have the advantage of probing different DM models through their characteristic spectral distributions. To make current and future DM searches more effective it is important to know in which energy band to focus the efforts in order to maximize the potential DM signal over the expected background. We dedicate this section to the spectral distribution of gamma-ray flux from clusters. The flux emerge from a DM LP model that emit final state radiation and give rise to substantial amounts of electrons and positrons that IC upscatter background radiation fields to high energies. We also consider a few supersymmetric

DM models with a high gamma-ray yield in the form of continuum emission and IC induced emission. In addition to the annihilating DM, we estimate the gamma-ray flux induced by shock accelerated CRps.

In Fig. 6 we show the differential flux from the Fornax cluster which is one of the best clusters for indirect DM searches due to its relative high DM induced fluxes and low CR induced fluxes. We derive the emission from four different supersymmetric BM models and compare the flux to both the emission induced by CRps as well as to the differential gamma-ray upper limits set by Fermi-LAT after 18 months of observations [54]. We find that the upper limits are not violated, although the predicted DM flux that is dominated by the continuum emission from K' and I' models (shown in the left panels) are close to the upper limits and can potentially be probed by the Fermi 3 year data. Furthermore, the expected masking gamma-ray signal induced by CRps is about a factor 10 below the DM continuum flux from the K' and I' BM models around 10 GeV. It is also important to note that IC emission from upscattered CMB and SD photons is at least a factor 10 lower than the expected flux from CRps above 100 MeV, making it very hard to distinguish such a signal from the foreground due to the similar spectral index. Furthermore, below the pion bump we expect the IC emission coming from shock accelerated electrons to be dominating [20]. Hence the IC emission from SUSY DM in clusters can for most applications safely be neglected compared to the CRps and DM continuum emission.

CONSIDER REWRITING, START WITH PHYSICS, THEN DISCUSS DOMINATING CONTRIBUTIONS, PEAKS, AND SPECTRAL INDICES

In Fig. 7 we show the total IC emission as well as its individual contributions from different IC upscattered radiation fields. The left panel show the gamma-ray emission from the LP model and the right panel from the K' BM model, and for comparison we overplot the emission expected from the CRps. Due to the flat electron and positron spectrum resulting from the DM LP model and the relative smaller energy density of the CMB compared to the SD, we find that the upscattered CMB photons dominate the total DM IC emission in the energy regime below 100 GeV, while the SD dominate above this energy. For the BM models this transition is shifted towards a smaller energy since the electron and positron spectrum has a steep spectral distribution that suppresses low energy photon fields. This suppression is also seen in the relative normalization of the flux where the IC from both CMB and dust photons are lower compared to the starlight simply because the starlight has a higher energy, hence it is upscattered by more abundant low energy electrons and positrons (c.f. Fig. 18). At the highest gamma-ray energies of about 100 GeV and above, the IC from starlight steepens because it both probes the high energy tail of the electrons as well as suffer from the KN suppression. Even though the SD component seems to be suppressed compared to the CMB at energies around 100 MeV, it has a relative large impact on the steady

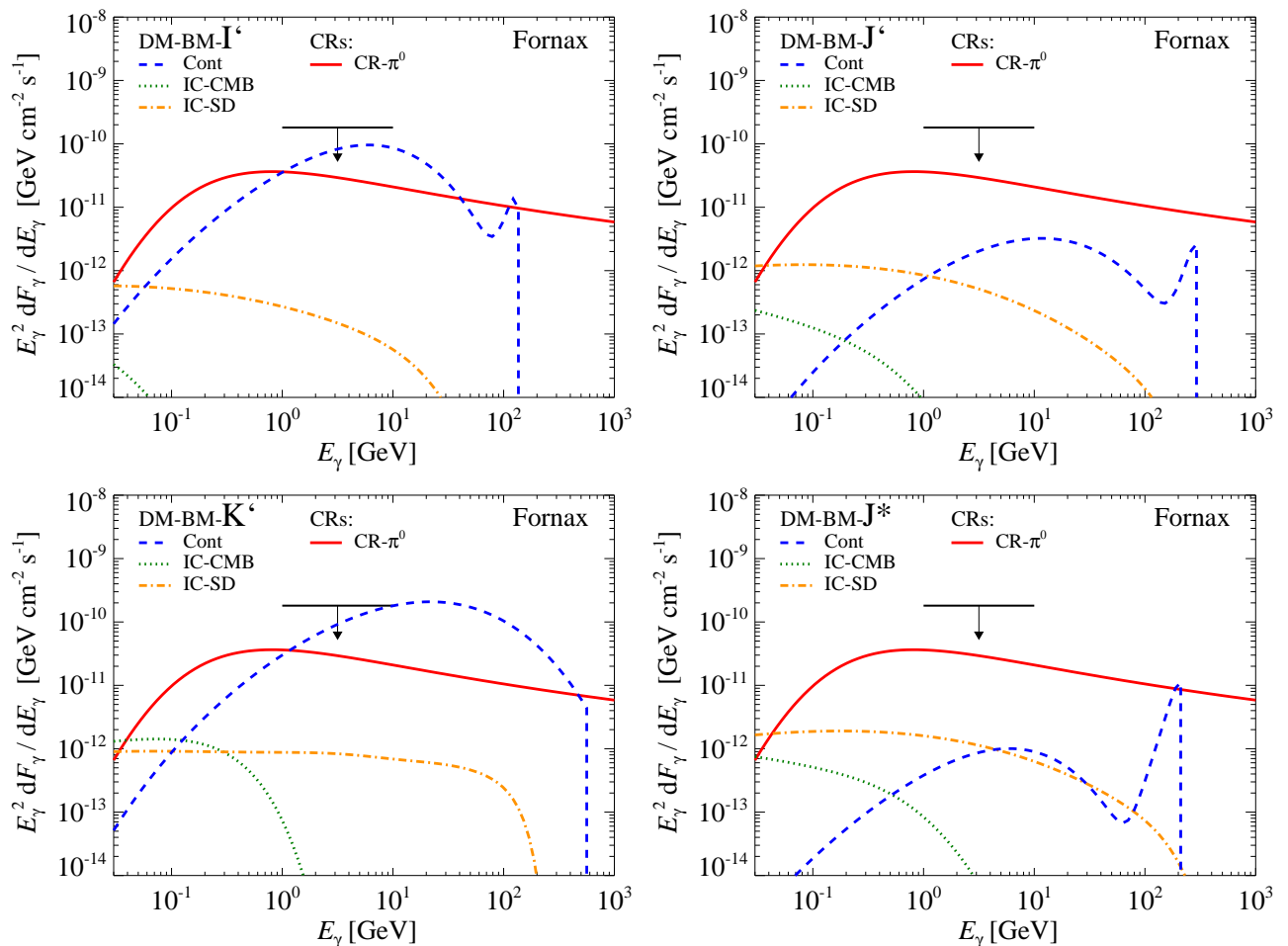


FIG. 6. Comparing the differential flux from different models: we show the continuum emission from DM benchmark (BM) models (blue dashed), electrons and positrons from DM BM models that inverse Compton upscattered both CMB photons (orange dash-dotted) as well as dust and star photons (green dotted), and CRp induced gamma-ray emission (red solid). Each panel is associated with an individual DM BM model; upper left I', lower left K', upper right J', and lower right J\*. The emission is calculated for the Fornax cluster using a point spread function of 0.1 deg and a boost from substructures of 570. We find bright prospects for detecting the continuum emission that is dominating the total emission in the GeV energy range. Also note that, above 100 MeV the total inverse Compton emission is at least a factor 10 smaller than the emission expected from both the continuum emission and the emission coming from CRps.

state electron spectrum. If we remove the SD cooling, we find a factor two larger IC flux at low energies for a cluster of the size of Fornax. For more massive clusters we expect a larger IC flux from the SD component, but a smaller contribution from the CMB because of the more effective cooling.

Because of the large boost factor for the LP model ( $\sim 10^4$ ), we overproduce the upper gamma-ray limit in the 1 – 10 GeV energy interval set by Fermi-LAT by about a factor 100. This imposes tight constraints on both the boost from substructures and the Sommerfeld enhancement. These constraints might improve with future more sensitive Cherenkov telescopes. However considering that an indirect detection of DM in clusters relies on the boost from substructures whose main contribution comes from the periphery, we conclude that the wide an-

gular extent of clusters in gamma-rays on the sky suggest that these sources are not ideal for Cherenkov telescopes due to the loss of sensitivity outside the small PSF (BETTER CHECK THIS WITH SOME EXPERT).

It is also interesting to compare the total contribution from the LP model, the brightest BM model, and the CRp induced emission. In Fig. 8 we show the integrated flux from Fornax for our different gamma-ray models and compare it to the unresolved integrated flux upper limit on Fornax set by Fermi-LAT where they averaged the flux over the energy range 0.2 – 100 GeV assuming a spectral index of 2. Again we are overproducing the upper limits, although only with a factor 10 which is about a order magnitude less constraining than the differential flux in the energy range 1 – 10 GeV. From the figure one clearly see that the LP model is dominating the entire gamma-

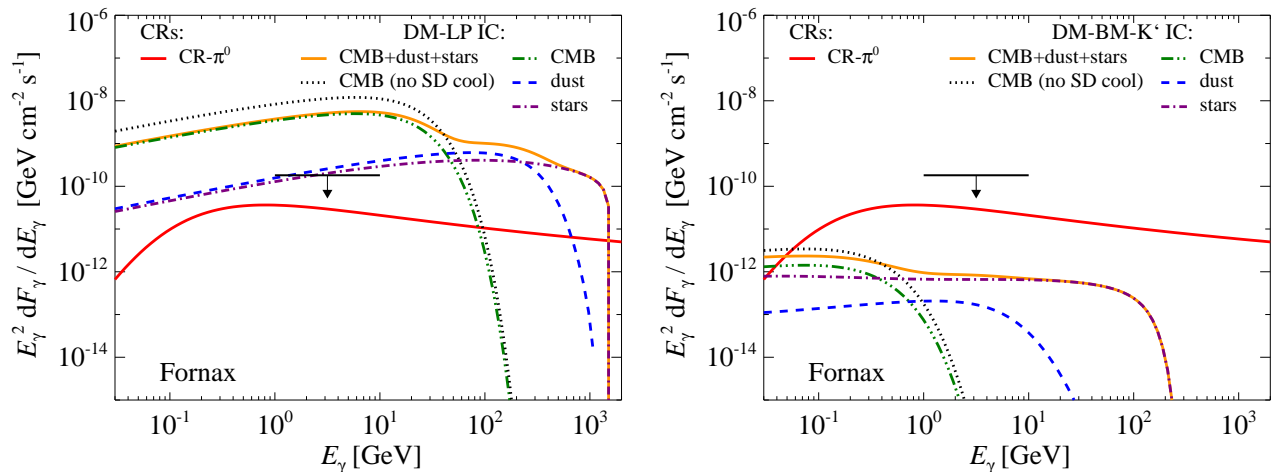


FIG. 7. Comparing the flux from different inverse Compton upscattered radiation fields. We show the differential inverse Compton emission induced by leptophilic DM in the left panel and by the  $K'$  benchmark model in the right panel. The contribution from each individual radiation field from top line to bottom line; CMB (green dashed-double-dotted), dust (blue dashed), stars (purple dashed-dotted). The sum of the three components are shown with the orange solid line. The black dotted line represents the upscattered CMB photons without any cooling from stars and dust. The red solid line show the CRp induced gamma-ray flux. The black arrow show the differential upper limit from Fermi [54]. All fluxes are calculated for the Fornax cluster within  $r_{200}$  using a point spread function of 0.1 deg. The boost from Sommerfeld and substructures is about 130 and 570, respectively.

ray energy range up to the DM mass of this model of about 1 TeV. In addition it is interesting to note that the flux the DM BM  $K'$  model is above the predicted emission from the CRps in the 1–100 GeV energy regime accessible both to Fermi and Cherenkov telescopes.

We continue by comparing how the estimated differential flux from Fornax to three other clusters in Fig. 9; the close by well studied Virgo cluster, the X-ray bright Perseus clusters, and the massive merging Coma cluster. We find high DM induced gamma-ray fluxes from both the Fornax and Virgo clusters, which highlight them as promising targets for indirect DM searches. Note, however, that we have used spatially unresolved upper limits, which is quite optimistic for the angular extended Virgo cluster. It is quite striking how constraining the upper limits for the Fornax cluster is compared to the other clusters, especially in the 1–10 GeV energy regime where Fermi-LAT is most sensitive due to the maximized effective area. The upper limits for Virgo and Perseus are background contaminated by AGN activity from M87 and NGC 1267, respectively, and do not gain much from the increased sensitivity. One should also note that the high CRp induced flux from both Coma and Perseus is of the same magnitude as the DM flux from LP models, making it difficult for indirect DM searches in those clusters. Conversely is the Fornax cluster a great target for indirect DM studies because the relative low gamma-ray flux from CRps, absents of an active AGN, and high DM gamma-ray flux. Actually, the Fermi-LAT 3 year data will be able to constrain the smallest mass of substructures using the DM BM models. We have also learned that close by clusters are superior to far away

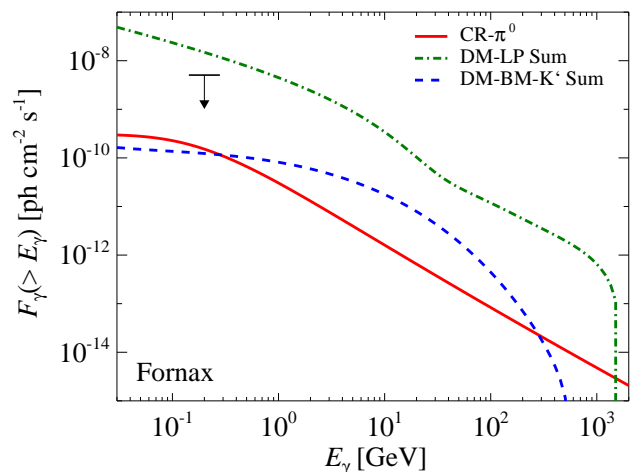


FIG. 8. Comparing the energy integrated flux from different models. We show the emission from; CRp induced emission (red solid), leptophilic models (LP) that include both final state radiation and IC upscattered CMB, dust and starlight (green dash-dotted), and benchmark  $K'$  models (BM) include continuum emission, and IC upscattered CMB, dust and starlight (blue dashed). The black arrow show the integrated flux upper limit set by Fermi-LAT. The emission is calculated for the Fornax cluster using a point spread function of 0.1 deg. The boost from Sommerfeld and substructures is about 130 and 570, respectively. We find that LP models are dominating the total flux in the entire energy range, where the IC upscattered CMB photons overproduce the upper limit by a factor 3.

clusters, even though close by clusters have a mass that is much smaller. In fact, we can understand this by looking at the luminosity-to-mass scaling relations. The gamma-ray luminosity from the smooth density profile is given by

$$L_{\text{sm}} \propto \int dV \rho(r)^2 \propto \frac{c^3}{[\log(1+c) - c/(1+c)]} \propto M_{200}^{0.83}, \quad (39)$$

and the total luminosity including boostfactors for the DM LP and BM models is given by

$$L_{\text{tot,LP}} = L_{\text{sm,LP}} B_{\text{LP}} \propto M_{200}^{0.73} \quad \text{and} \quad (40)$$

$$L_{\text{tot,BM}} = L_{\text{sm,BM}} B_{\text{BM}} \propto M_{200}^{1.06}, \quad \text{where} \quad (41)$$

$$B_{\text{LP}} = B_{\text{sfe}} B_{\text{sub}} \propto M_{200}^{-1/3} M_{200}^{0.23} \propto M_{200}^{-0.1}, \quad (42)$$

$$B_{\text{BM}} = B_{\text{sub}} \propto M_{200}^{0.23}. \quad (43)$$

Hence increasing the mass with a factor two doubles the luminosity, but increasing the distance by a factor two decrease the flux with a factor four. **(DELETED TEXT)**

As we have seen in this section the LP models overproduce both the differential and integrated flux upper limits set by the Fermi-LAT for several clusters. We can use these upper limits to enforce constraints on the SFE and boost from substructures. As more sensitive experiments and better upper limits emerge, we can start ruling out models giving rise to these type of boost factors that are manifested in the gamma-ray flux. Especially interesting is to constrain the SFE, where a boost of 300 is required to explain the excess of electrons and positrons observed in the vicinity of Earth by PAMELA/Fermi/HESS. In Fig. 9 we use the estimated flux from four clusters to constrain the minimum mass of substructures where  $M_{\text{lim}} \propto M_{200}^{0.226}$ , as well as the SFE. As expected, the Fornax cluster is the most constraining cluster by far, although the current upper limits are not good enough to rule out either the boost from substructures or SFE. Assuming that the electron and positron excess is due to SFE DM matter, then in order not to overproduce the differential upper limits set by Fermi-LAT in the energy range 1–10 GeV [55] we can constrain the smallest mass of substructures to  $M_{\text{lim}} \gtrsim 10 M_{\odot}$ . Instead assuming the standard mass of the smallest substructures of  $M_{\text{lim}} \gtrsim 10^{-6} M_{\odot}$ , we can constrain the boost from SFE to about 4 in Fornax, corresponding to a maximum SFE in the MW of about 10.

HOW ARE UL CALCULATED?

#### IV. SURFACE BRIGHTNESS PROFILES

The large angular extent of clusters on the sky in combination with the small PSF of most gamma-ray probes ( $\sim 0.1$  deg) suggest that we would be able to probe the different spatial regimes of a cluster. Especially important is the spatial distribution of the gamma-ray emission as it bias upper limits derived for spatially extended clusters where a simple density profile is often assumed.

In fact when DM substructures are included the total brightness profile is almost flat and very different from the smooth halo distribution with a steep outer brightness slope of  $-5$ .

In this section we investigate the gamma-ray surface brightness profiles induced by both DM and CRps. We start by comparing the substructure included brightness from different clusters in Fig. 11. As expected, we find that the DM flux in all clusters follow the same smooth shape imposed by the substructures. Even as far in as 1% of  $r_{200}$  we are dominated by the substructures, which is due to the projection of the outer cluster halo (see Sect. II A 1 for a longer discussion). This implies that the spatial distribution of annihilating DM induced emission is independent of the type of DM model, and can not be used to separate different models. The normalization for the BM model determined by  $B_{\text{sub}} L_{\text{BM}}^{1/3} \propto M_{200}^{0.50}$ , which explains the factor three difference in normalization. The flux from the LP model show a smaller spread in the normalization which is due to the additional contribution from SFE with a negative mass trend, hence a normalization with a softer mass-scaling of  $\sim M_{200}^{0.17}$ . The surface brightness induced by CRps mainly trace the gas profile of each cluster with an additional enhancement in the center due to the expected large population of CRps, hence we see a much larger spread in these profiles. It is noticeable that Fornax show such a small surface brightness. However, it is explained by the low gas density outside the BCG and the less abundant CRp population in the relative small cluster compared to a more massive cluster [20]. In fact, only the very inner part of Fornax is dominated by a large gamma-ray flux from CRps, which however, is negligible compared to the flux withing  $r_{200}$ . This is the reason why Fornax is such a good target for indirect DM searches, and competitive to DM searches in dwarf galaxies. Although, it might be a problem for Cherenkov telescopes looking for a DM in the center of Fornax.

To quantify the impact of substructures on the spatial profiles in more detail we again turn to the Fornax clusters and show in Fig. 12 a comparison of surface brightness profiles with and without substructures. It is quite remarkable how flat the profiles including substructures are compared to the ones without. This implies that the relative flux within the PSF in the center is comparable to the outer parts, which should increase the signal-to-noise significantly. If we assume that substructures for some reason are suppressed in the Fornax cluster, then the expected signal from DM is swamped by astrophysical backgrounds over the entire extent of the cluster, even though Fornax has one of the highest ratios of DM/CRp gamma-ray brightness.

In order to learn about the spatial distribution of the DM flux in various clusters for different DM models and associated gamma-ray components, we show in the left panel of Fig. 13 the brightness profiles for the smooth DM distribution for the same four representative clusters that was shown previously in Fig. 11. In addition, we



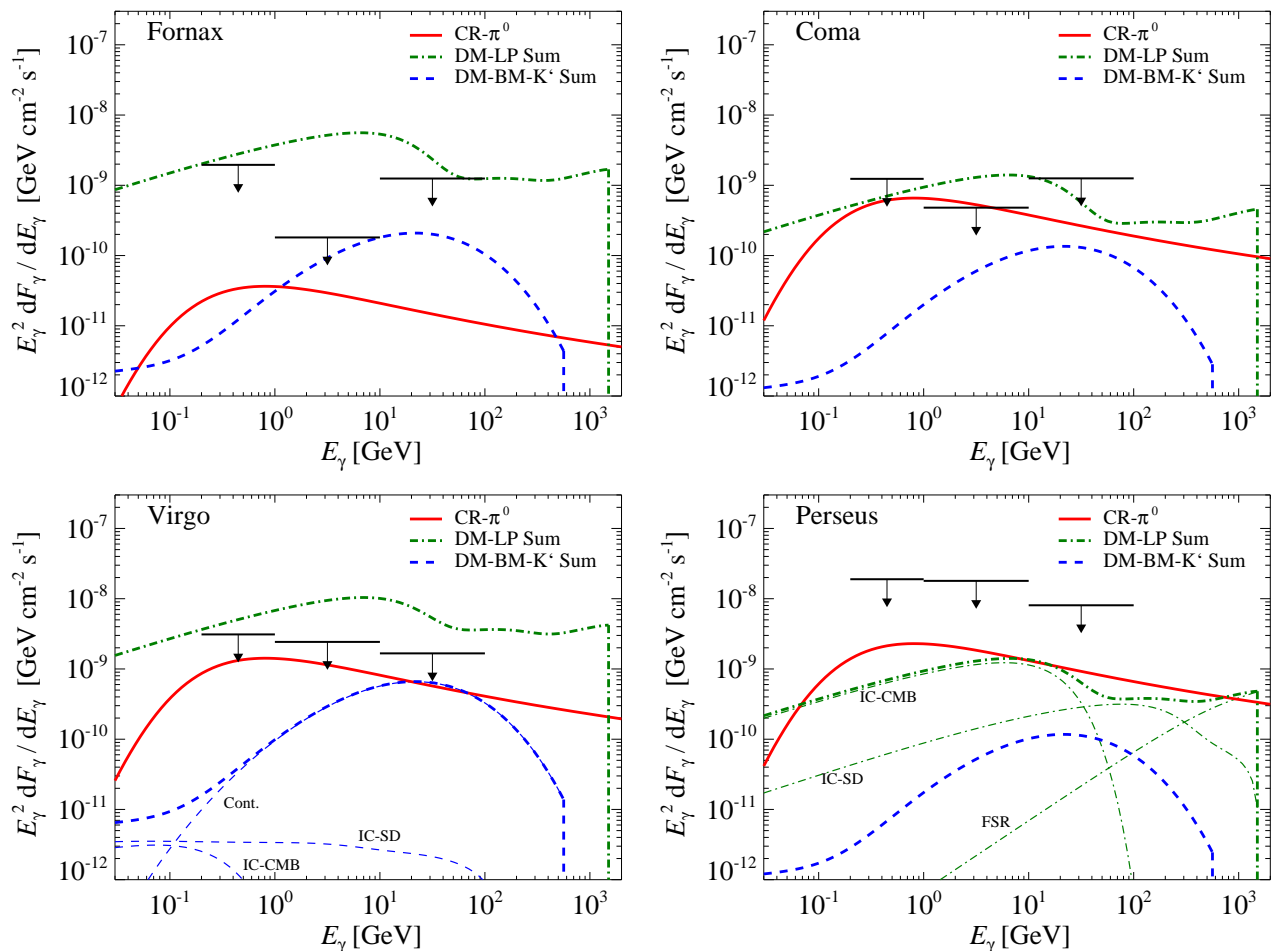


FIG. 9. Comparing the emission from different clusters. We show the differential flux from four clusters; Fornax (upper left), Coma (upper right), Virgo (lower left), and Perseus (lower right). The different flux models; CRp induced emission (red solid), leptophilic models (LP) include both final state radiation and IC upscattered CMB, dust and starlight (green dash-dotted), and benchmark K' models (BM) include continuum emission, and IC upscattered CMB, dust and starlight (blue dashed). The arrows have colors matching each cluster and show the differential upper limits set by Fermi-LAT in the energy ranges 0.2 – 1 GeV, 1 – 10 GeV, and 10 – 100 GeV from left to right. For visualization we offset the arrows by increasing the mean energy by 30% in the opposite order as they appear in the figure, i.e. starting with Perseus. The flux from the clusters is integrated out to  $r_{200}$  using a point spread function of 0.1 deg and includes the boost from substructures. We find that the lower GeV energy regime is most constraining, and induce upper limits on boost factors.

show the spatial dependence of the individual gamma-ray components for the Fornax cluster in the right panel. We find that the spatial distribution of the DM emission at 1 GeV in the outer parts of the all clusters have the same shape. The shape trace the underlying density slope of  $-3$ , which is expected for IC upscattered CMB photons. This picture is confirmed by the components study in the right panel that show the negligible contribution from the IC upscattered light from stars and dust at this energy. Since the surface brightness from BM models are dominated by the continuum emission at each radius in all clusters, we see that this component follows the projected density profile over the entire clusters. The LP model, however, show a much flatter profile in the central parts of the clusters, which is due to the efficient IC cooling of

the electrons and positrons on the SD component. There is also some variation in the profiles for the different clusters in the central parts. Especially in the Fornax cluster, where we find a factor two larger flux compared to the other clusters. This is due to more efficient SD cooling of the dominating IC upscattered CMB photons in Fornax; a low X-ray luminous cluster has a low energy density in starlight and dust in our semi-analytic SD model. However, note that the surface brightness from the SD component is suppressed at the relative low energy of 1 GeV. Since there is no enhancement from the substructures, the overall mass normalization of the LP DM model has a marginally negative trend  $\sim M_{200}^{-0.06}$ . Hence, we only see a very small difference in outer parts of the different clusters from these type of models. The BM DM mod-

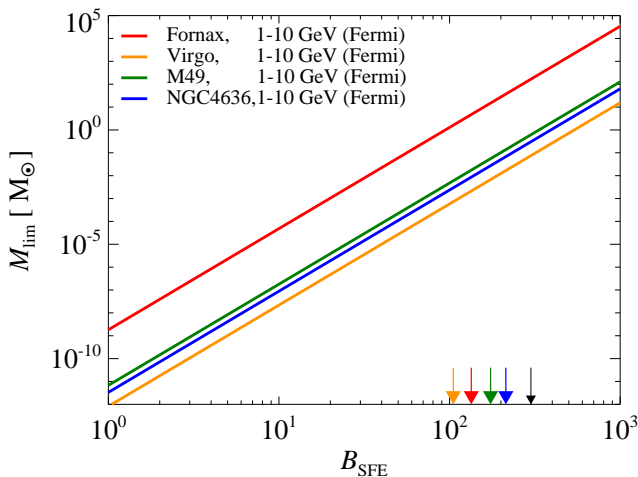


FIG. 10. Constraining boost factors using flux upper limits. The leptophilic (LP) gamma-ray emission is derived within  $r_{200}$  using a point spread function of 0.1 deg. In order not to overproduce the Fermi-LAT differential flux upper limits in the energy interval 1 – 10 GeV the boost from substructures and Sommerfeld enhancement (SFE) is constrained for four clusters; Fornax (red), Virgo (orange), M49 (green), and NGC4636 (Blue). The SFE has been rescaled from 300 (refer to equation) that is required to explain the electron and positron excess observed at Earth with LP DM (black arrow). If the DM interpretation is correct, we can constrain the smallest size of halos to be larger than  $10 M_\odot$ . However, if the smallest size of DM halos is  $10^{-6} M_\odot$ , we can constrain the SFE to about 4 in Fornax, corresponding to a maximum SFE in the MW of about 10.

els have a normalization of  $\sim M_{200}^{0.27}$ , hence more massive clusters show a slightly higher surface brightness. As also noticed in previous figure, the flux from DM is dominated by the CRp induced emission for all clusters.

Might want to mention that the IC-SD spectra for both DM models follow the projected density contribution due to the cancellation in the radial dependence of the SD spectra and the SD cooling that dominates the cooling in the center.

In Sect. IV we saw that the spectral distribution of the gamma-ray flux from the LP model were dominated at high energies of 100 GeV by final state radiation and the IC upscattered starlight and dust, while the BM models were mainly dominated by the continuum emission. These high energies are reachable by both Fermi-LAT and Cherenkov telescopes, thus important observationally. We therefore show in Fig. 14 the surface brightness above 100 GeV for a realistic PSF of 0.1 deg where we include the boost from substructures. We look at both the relative small Fornax cluster and the massive close by Virgo cluster. Both clusters show a very flat brightness profile within about 10% of  $r_{200}$ , due to both the effect from substructures and the smoothening over the PSF. The CRp induced emission also show a smoothening in the central parts due to the PSF. In the outer part of the Fornax cluster the CRp flux is suppressed com-

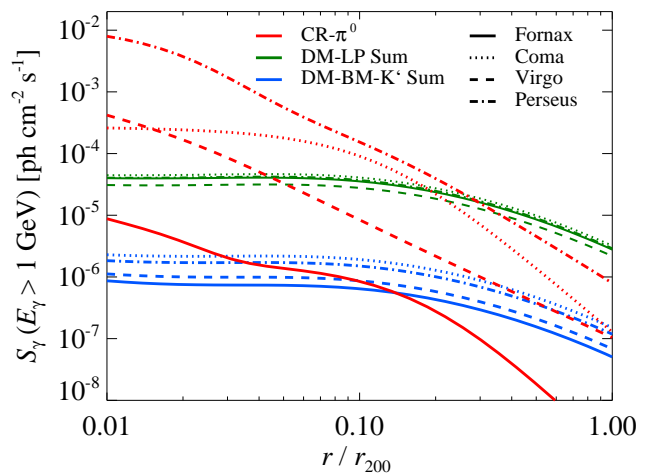


FIG. 11. Comparing the surface brightness from different clusters. We show the CRp induced emission (red), leptophilic emission (green), and emission from the K' benchmark model (blue). The surface brightness above 1 GeV is derived using a very small point spread function ( $\theta_{\text{psf}} = 10^{-5}$  deg). The different line styles each represent a cluster; Fornax (solid), Coma (dotted), Virgo (dashed), and Perseus (dash-dotted). The boost from Sommerfeld and substructures is about 130 and 570, respectively. Notice the very similar shape and normalization of the DM models, while the CRps have a much larger scatter in the profiles.

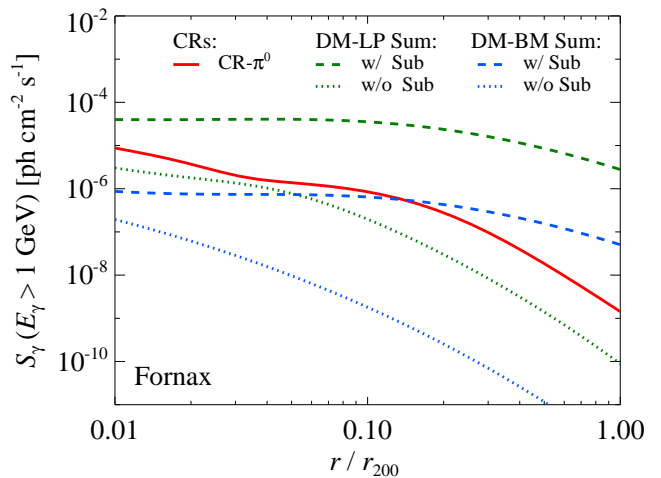


FIG. 12. The impact of substructures on surface brightness. We show the surface brightness at 1 GeV for the Fornax cluster using a very small point spread function of  $10^{-5}$  deg that reveals the details of the spatial profiles. The emission induced by CRps is denoted by the red solid line, the leptophilic models by green lines, and the DM K' benchmark model by blue lines. The dashed line show the brightness where the boost from substructures is included while the substructures are excluded in the dotted line. The boost from Sommerfeld and substructures is about 130 and 570, respectively. Notice the nearly flat profiles when substructures are included, and the relative large boost at a percent of  $r_{200}$ .

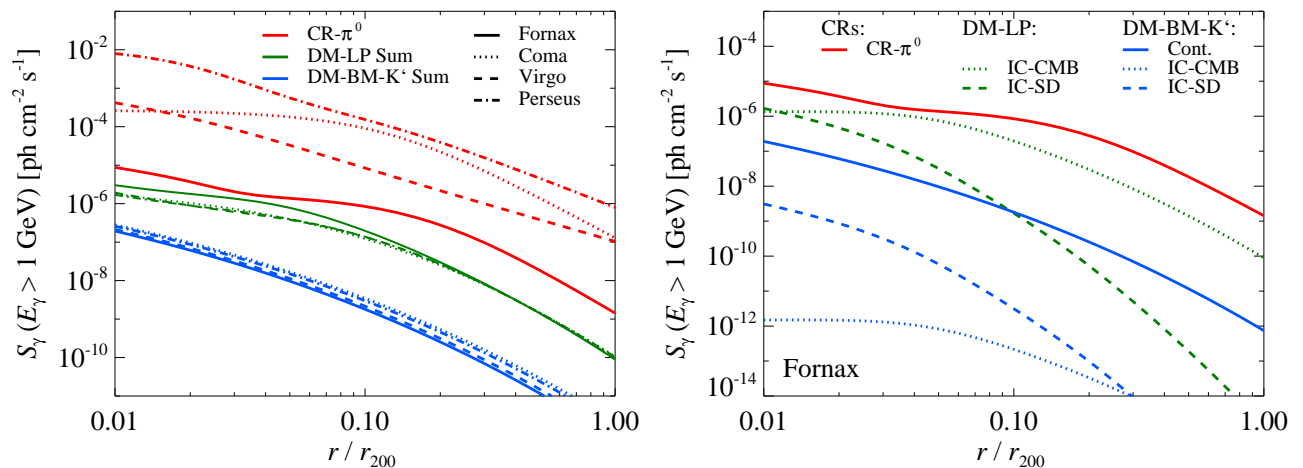


FIG. 13. The surface brightness without substructures. We show the CRp induced emission (red), leptophilic emission (green), and emission from the  $K'$  benchmark model (blue). The surface brightness above 1 GeV is derived using a very small point spread function ( $\theta_{\text{psf}} = 10^{-5}$  deg). LEFT PANEL: compare the surface brightness for different clusters; Fornax (solid), Coma (dotted), Virgo (dashed), and Perseus (dash-dotted). RIGHT PANEL: compare different emission components in Fornax; dotted lines show the inverse Compton (IC) upscattered CMB photons, dashed lines show the IC upscattered photons from stars and dust, and blue solid line show the continuum emission from the  $K'$  benchmark model.

pared to the substructure boosted DM flux, where the LP model is over three orders of magnitude larger. Although, it should be noted that there are large uncertainties in the gas density profile used to estimate the CRp surface brightness (see Fig. 19 for more details).

## V. PREDICTIONS AND OBSERVATIONAL LIMITS

### Model predictions

difficult to detect DM without a Sommerfeld boost with Cherenkov telescopes since the boost from substructures is extended while the sensitivity of Cherenkov telescopes drops linearly with radius outside the point spread function (CHECK)

we rule out the leptophilic models in present form in 14 clusters, and limit the boost from Sommerfeld enhancement in the MW to less than 10

mention prime cluster candidates, LP under pressure, Fornax start being constraining, since only few clusters close to UL stacking will not increase the DM limits much

the tightest limits on DM and CRps from Fermi are in the 1-10 GeV regime, where Fornax, M49, and NGC4636 are the most constraining "clusters" for the DM and Virgo, Coma and Norma are very close to the predictions for the CRps

using beta profiles, discrepancy with Norma cluster in Ackermann gone, Integrated flux similar

AGN M87, effective area better in 1 GeV range

## VI. CONCLUSIONS

Some of the results (should discuss what we want to emphasize): –) the flux from annihilating DM is boosted by about a factor 1000 in clusters –) flat surface brightness profiles with substructures –) Fornax is a great target for indirect DM studies because the relative low flux from CRps and high flux from DM –) the IC upscattered photons from stars and dust are dominated in the relevant energy regimes by the continuum emission for our DM benchmark models –) Fermi 3 year data will constrain the smallest mass of substructures using the benchmark models –) difficult to detect DM without a Sommerfeld boost with Cherenkov telescopes since the boost from substructures is extended while the sensitivity of Cherenkov telescopes drops linearly with radius outside the point spread function (CHECK) –) we rule out the leptophilic models in present form in 14 clusters, and limit the boost from Sommerfeld enhancement in the MW to less than 10 –) the tightest limits on DM and CRps from Fermi are in the 1-10 GeV regime, where Fornax, M49, and NGC4636 are the most constraining "clusters" for the DM and Virgo, Coma and Norma are very close to the predictions for the CRps –) we provide a rather simple model to calculate the spatial and spectral distribution of dust and stars in cluster (might be used for galaxies? with different spatial profile)

Anders Pinzke acknowledges NSF grant AST 0908480 for support.

[1] M. Pato, L. Baudis, G. Bertone, R. R. de Austri, L. E. Strigari, *et al.*, (2010), \* Temporary entry \*,

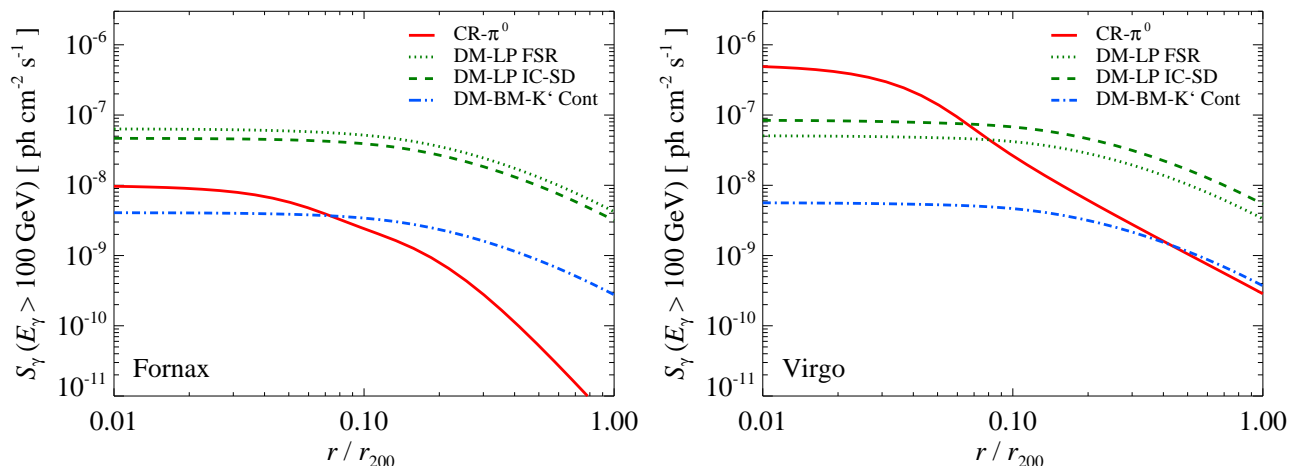


FIG. 14. Surface brightness predicted for Cherenkov telescopes at high energies. We show the emission above 100 GeV and include the boost from substructures. We use a point spread function of 0.1 deg that is typical for both Cherenkov telescopes as well as the Fermi-LAT at this energy. Left panel show the Fornax cluster and right panel the Virgo cluster. The gamma-ray emission is derived for the following components; CRps (red solid), continuum emission from the DM K' benchmark model (blue dash-dotted), as well as final state radiation (green dashed) and inverse Compton upscattered dust and starlight (green dotted) from leptophilic DM.

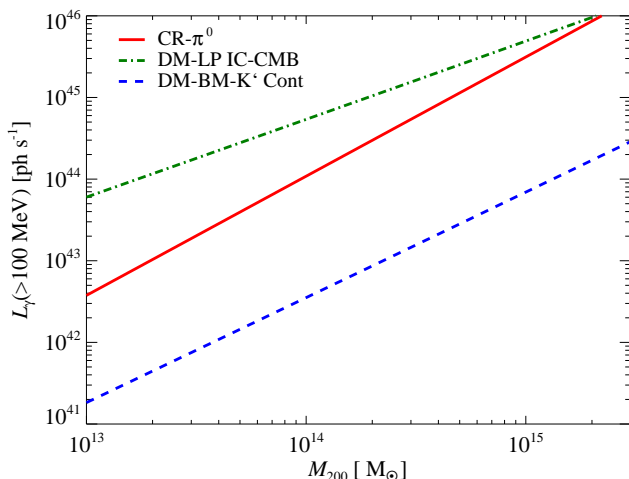


FIG. 15. Lum-scaling relations, mass dependence of SD cooling have been neglected, actually a factor few difference for groups. factor 2 for Fornax, and small difference for large clusters

- [2] J. R. Ellis, J. L. Feng, A. Ferstl, K. T. Matchev, and K. A. Olive, *Eur.Phys.J.* **C24**, 311 (2002), arXiv:astro-ph/0110225 [astro-ph].
- [3] H. Baer, A. Mustafayev, S. Profumo, and X. Tata, *Phys.Rev.* **D75**, 035004 (2007), arXiv:hep-ph/0610154 [hep-ph].
- [4] V. Khachatryan *et al.* (CMS Collaboration), (2011), \* Temporary entry \*, arXiv:1101.1628 [hep-ex].
- [5] L. Bergstrom, *New J.Phys.* **11**, 105006 (2009), arXiv:0903.4849 [hep-ph].
- [6] CTA, (2010), The CTA Consortium: Design Concepts for the Cherenkov Telescope Array, arXiv:1008.3703 [astro-ph.IM].
- [7] L. Bergstrom, T. Bringmann, and J. Edsjo, (2010), \* Temporary entry \*, arXiv:1011.4514 [hep-ph].
- [8] D. Hooper and L. Goodenough, *ArXiv e-prints* (2010), arXiv:1010.2752 [hep-ph].
- [9] A. Boyarsky, D. Malyshev, and O. Ruchayskiy, *ArXiv e-prints* (2010), arXiv:1012.5839 [hep-ph].
- [10] T. Bringmann, M. Doro, and M. Fornasa, *JCAP* **1**, 16 (2009), arXiv:0809.2269.
- [11] V. A. Acciari, T. Arlen, T. Aune, M. Beilicke, W. Benbow, D. Boltuch, S. M. Bradbury, J. H. Buckley, V. Bugaev, K. Byrum, A. Cannon, A. Cesarini, J. L. Christiansen, L. Ciupik, W. Cui, R. Dickherber, C. Duke, J. P. Finley, G. Finnegan, A. Furniss, N. Galante, S. Godambe, J. Grube, R. Guenette, G. Gyuk, D. Hanna, J. Holder, C. M. Hui, T. B. Humensky, A. Imran, P. Kaaret, N. Karlsson, M. Kertzman, D. Kieda, A. Konopelko, H. Krawczynski, F. Krennrich, G. Maier, S. McArthur, A. McCann, M. McCutcheon, P. Moriarty, R. A. Ong, A. N. Otte, D. Pandel, J. S. Perkins, M. Pohl, J. Quinn, K. Ragan, L. C. Reyes, P. T. Reynolds, E. Roache, H. J. Rose, M. Schroedter, G. H. Sembroski, G. D. Senturk, A. W. Smith, D. Steele, S. P. Swordy, G. Tešić, M. Theiling, S. Thibadeau, A. Varlotta, V. V. Vassiliev, S. Vincent, R. G. Wagner, S. P. Wakely, J. E. Ward, T. C. Weekes, A. Weinstein, T. Weisgarber, D. A. Williams, S. Wissel, B. Zitzer, and VERITAS Collaboration, *Astrophys. J.* **720**, 1174 (2010), arXiv:1006.5955 [astro-ph.CO].
- [12] P. Scott, J. Conrad, J. Edsjö, L. Bergström, C. Farnier, and Y. Akrami, *JCAP* **1**, 31 (2010), arXiv:0909.3300 [astro-ph.CO].
- [13] M.-L. Garde, Talk at IDM10, Montpellier, France, July 2010, to appear in the Proceedings.
- [14] A. Pinzke, C. Pfrommer, and L. Bergström, *Physical Review Letters* **103**, 181302 (2009), arXiv:0905.1948 [astro-ph.HE].
- [15] L. Gao, C. S. Frenk, M. Boylan-Kolchin, A. Jenkins,



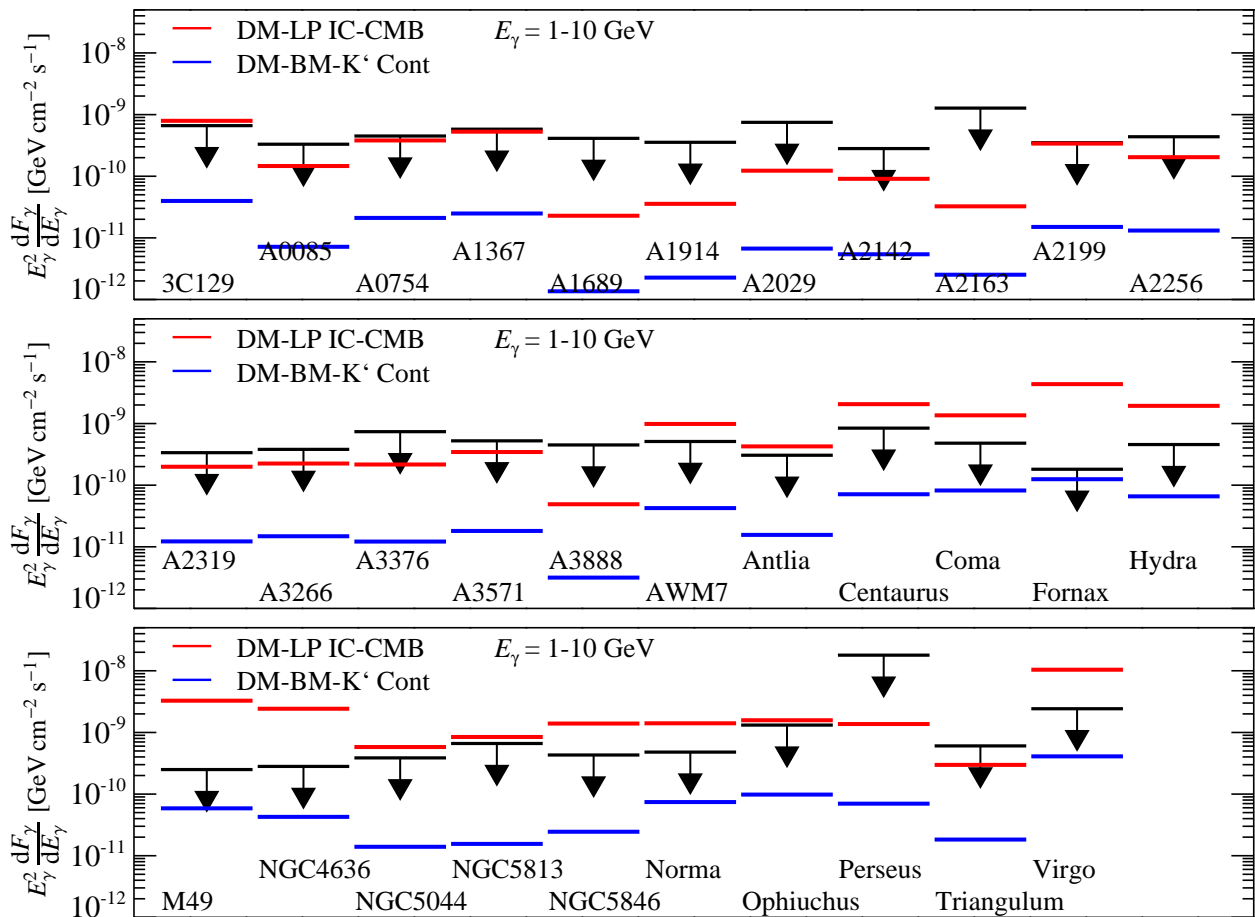


FIG. 16. *Fermi flux upper limits contrasted to the predicted DM gamma-ray flux. We show the mean differential flux in the energy range  $E_\gamma = 1 - 10$  GeV for 32 clusters. The Fermi-LAT upper limits are shown with black arrows. The predicted fluxes are derived from both a leptophilic DM model that result in inverse Compton upscattered CMB photons (red), and the continuum emission from the DM K' benchmark model (blue). The leptophilic fluxes are ruled out by 14 of the clusters, with the strongest constraints set by Fornax and M49. We can not constrain the benchmark models, although our predictions are approaching the upper limits.*

- V. Springel, and S. D. M. White, MNRAS **410**, 2309 (2011), arXiv:1006.2882 [astro-ph.CO].
- [16] All halo masses and length scales in this paper are scaled to the currently favored value of Hubble's constant,  $H_0 = 70 \text{ km s}^{-1} \text{ Mpc}^{-1}$ . We define the virial mass  $M_{200}$  and virial radius  $r_{200}$  as the mass and radius of a sphere enclosing a mean density that is 200 times the critical density of the Universe  $\rho_{\text{cr}}$ .
- [17] L. Gao, S. D. M. White, A. Jenkins, F. Stoehr, and V. Springel, MNRAS **355**, 819 (2004), arXiv:astro-ph/0404589.
- [18] S. Colafrancesco, S. Profumo, and P. Ullio, A&A **455**, 21 (2006), arXiv:astro-ph/0507575.
- [19] T. E. Jeltema, J. Kehayias, and S. Profumo, Phys. Rev. D **80**, 023005 (2009), arXiv:0812.0597.
- [20] A. Pinzke and C. Pfrommer, MNRAS **409**, 449 (2010), arXiv:1001.5023 [astro-ph.CO].
- [21] A. V. Macciò, A. A. Dutton, and F. C. van den Bosch, MNRAS **391**, 1940 (2008), arXiv:0805.1926.
- [22] D. H. Zhao, Y. P. Jing, H. J. Mo, and G. Börner, Astrophys. J. **707**, 354 (2009), arXiv:0811.0828.
- [23] W. Hu and A. V. Kravtsov, Astrophys. J. **584**, 702 (2003), arXiv:astro-ph/0203169.
- [24] J. F. Navarro, A. Ludlow, V. Springel, J. Wang, M. Vogelsberger, S. D. M. White, A. Jenkins, C. S. Frenk, and A. Helmi, MNRAS **402**, 21 (2010), arXiv:0810.1522.
- [25] A. B. Newman, T. Treu, R. S. Ellis, and D. J. Sand, ApJL **728**, L39+ (2011), arXiv:1101.3553 [astro-ph.CO].
- [26] V. Springel, J. Wang, M. Vogelsberger, A. Ludlow, A. Jenkins, A. Helmi, J. F. Navarro, C. S. Frenk, and S. D. M. White, MNRAS **391**, 1685 (2008), arXiv:0809.0898.
- [27] M. Kuhlen, J. Diemand, P. Madau, and M. Zemp, Journal of Physics Conference Series **125**, 012008 (2008), arXiv:0810.3614.
- [28] Our approach of fitting the scaling behavior of  $L_{\text{sub}}(< r)$  directly from numerical simulations self-consistently accounts for the radial dependence of the substructure

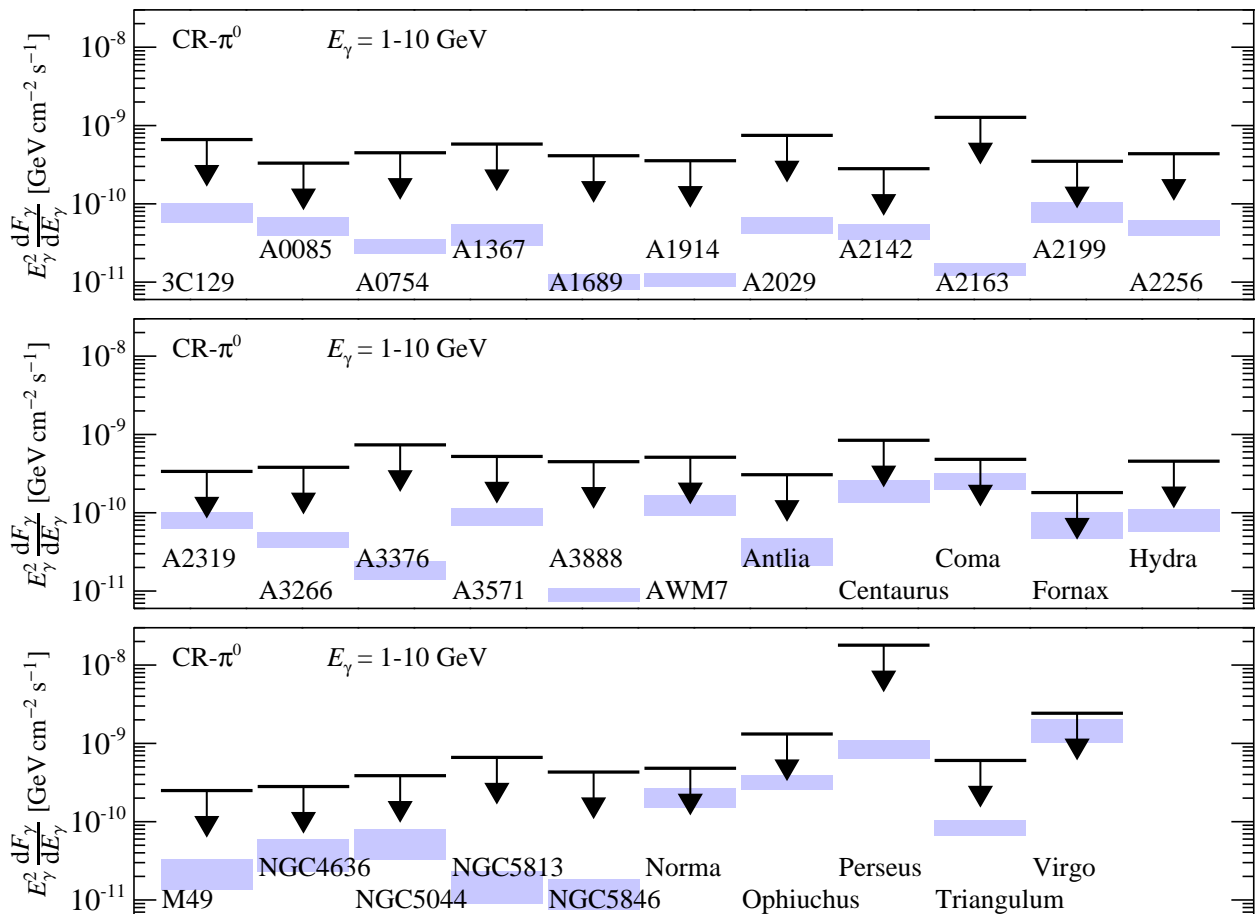


FIG. 17. *Fermi*-LAT flux upper limits contrasted to the predictions by the semi-analytic Pinzke and Pfrommer model for CRp induced gamma-ray emission. We show the mean differential flux in the energy range  $E_\gamma = 1-10$  GeV for 32 clusters. The *Fermi* upper limits are shown with black arrows. The blue boxes show the gamma-ray emission from CRp induced  $\pi^0$  decaying, where the upper bound shows the estimates for an optimistic model and the lower bound a more conservative model excluding point sources (the realistic case is more likely in between, see [20] for details). Note that there is currently no tension between our predictions and upper limits from *Fermi*, although *Virgo*, *Norma*, and *Coma* are close and will in the coming years enforce constraints on the hadronic models.

- concentration [26].
- [29] V. Springel, S. D. M. White, C. S. Frenk, J. F. Navarro, A. Jenkins, M. Vogelsberger, J. Wang, A. Ludlow, and A. Helmi, *Nature* (London) **456**, 73 (2008), arXiv:0809.0894.
  - [30] S. Hofmann, D. J. Schwarz, and H. Stöcker, *Phys. Rev. D* **64**, 083507 (2001), arXiv:astro-ph/0104173.
  - [31] A. M. Green, S. Hofmann, and D. J. Schwarz, *JCAP* **8**, 3 (2005), arXiv:astro-ph/0503387.
  - [32] J. C. Kempner, E. L. Blanton, T. E. Clarke, T. A. Enßlin, M. Johnston-Hollitt, and L. Rudnick, in *The Riddle of Cooling Flows in Galaxies and Clusters of galaxies*, edited by T. Reiprich, J. Kempner, N. Soker (2004) pp. 335–+, arXiv:astro-ph/0310263.
  - [33] L. Feretti, in *Astronomical Society of the Pacific Conference Series*, Astronomical Society of the Pacific Conference Series, Vol. 301, edited by S. Bowyer and C.-Y. Hwang (2003) pp. 143–+.
  - [34] C. Ferrari, F. Govoni, S. Schindler, A. M. Bykov, and Y. Rephaeli, *Space Science Reviews* **134**, 93 (2008), arXiv:0801.0985.
  - [35] V. S. Berezinsky, P. Blasi, and V. S. Ptuskin, *Astrophys. J.* **487**, 529 (1997).
  - [36] M. Jubelgas, V. Springel, T. Enßlin, and C. Pfrommer, *A&A* **481**, 33 (2008), arXiv:astro-ph/0603485.
  - [37] T. A. Enßlin, C. Pfrommer, V. Springel, and M. Jubelgas, *A&A* **473**, 41 (2007), arXiv:astro-ph/0603484.
  - [38] C. Pfrommer, V. Springel, T. A. Enßlin, and M. Jubelgas, *MNRAS* **367**, 113 (2006), arXiv:astro-ph/0603483.
  - [39] E. A. Helder, J. Vink, C. G. Bassa, A. Bamba, J. A. M. Bleeker, S. Funk, P. Ghavamian, K. J. van der Heyden, F. Verbunt, and R. Yamazaki, *Science* **325**, 719 (2009), arXiv:0906.4553 [astro-ph.GA].
  - [40] H. Kang and T. W. Jones, *Astrophys. J.* **620**, 44 (2005).
  - [41] T. Bringmann, L. Bergström, and J. Edsjö, *Journal of High Energy Physics* **1**, 49 (2008), arXiv:0710.3169 [hep-

- ph].
- [42] G. B. Rybicki and A. P. Lightman, *Radiative processes in astrophysics* (New York, Wiley-Interscience, 1979., 1979).
  - [43] G. R. Blumenthal and R. J. Gould, *Reviews of Modern Physics* **42**, 237 (1970).
  - [44] T. A. Porter, I. V. Moskalenko, and A. W. Strong, *ApJL* **648**, L29 (2006), arXiv:astro-ph/0607344.
  - [45] R. C. Gilmore, P. Madau, J. R. Primack, R. S. Somerville, and F. Haardt, *MNRAS* **399**, 1694 (2009), arXiv:0905.1144 [astro-ph.CO].
  - [46] S. Zibetti, S. D. M. White, D. P. Schneider, and J. Brinkmann, *MNRAS* **358**, 949 (2005), arXiv:astro-ph/0501194.
  - [47] M. Giard, L. Montier, E. Pointecouteau, and E. Simmat, *A&A* **490**, 547 (2008), arXiv:0808.2404.
  - [48] T. H. Reiprich and H. Böhringer, *Astrophys. J.* **567**, 716 (2002), arXiv:astro-ph/0111285.
  - [49] The measured brightness is converted into units of  $\text{erg s}^{-1}$  using  $[?] S(\text{mag}''^{-2}) = \mathcal{M}_{\odot} + 21.572 - 2.5 \log_{10} S(L_{\odot} \text{ pc}^{-2})$ , where the sun's absolute magnitude in the  $r$ -band is given by  $\mathcal{M}_{\odot} = 27.1 [?]$  and the luminosity of the sun by  $L_{\odot} = 3.85 \times 10^{33} \text{ erg s}^{-1}$ .
  - [50] C. Pfrommer and T. A. Enßlin, *A&A* **413**, 17 (2004).
  - [51] M. Abramowitz and I. A. Stegun, *Handbook of mathematical functions* (Dover, New York, 1965).
  - [52] G. W. Pratt, J. H. Croston, M. Arnaud, and H. Böhringer, *A&A* **498**, 361 (2009), arXiv:0809.3784.
  - [53] We derive the factor 1.58 using  $M_{200}/M_{500}$  for the clusters in the HIFLUGCS catalogue with a mass similar to  $M_{200} = 4.0 \times 10^{13} M_{\odot}$  that we use to derive the luminosity from dust.
  - [54] M. Ackermann, M. Ajello, A. Allafort, L. Baldini, J. Ballet, G. Barbiellini, D. Bastieri, K. Bechtol, R. Bellazzini, R. D. Blandford, P. Blasi, E. D. Bloom, E. Bonamente, A. W. Borgland, A. Bouvier, T. J. Brandt, J. Bregeon, M. Brigida, P. Bruel, R. Buehler, S. Buson, G. A. Caliandro, R. A. Cameron, P. A. Caraveo, S. Carrigan, J. M. Casandjian, E. Cavazzuti, C. Cecchi, Ö. Çelik, E. Charles, A. Chekhtman, C. C. Cheung, J. Chiang, S. Ciprini, R. Claus, J. Cohen-Tanugi, S. Colafrancesco, L. R. Cominsky, J. Conrad, C. D. Dermer, F. de Palma, E. d. C. e. Silva, P. S. Drell, R. Dubois, D. Dumora, Y. Edmonds, C. Farnier, C. Favuzzi, M. Frailis, Y. Fukazawa, S. Funk, P. Fusco, F. Gargano, D. Gasparrini, N. Gehrels, S. Germani, N. Giglietto, F. Giordano, M. Giroletti, T. Glanzman, G. Godfrey, I. A. Grenier, M. Grondin, S. Guiriec, D. Hadasch, A. K. Harding, M. Hayashida, E. Hays, D. Horan, R. E. Hughes, T. E. Jeltema, G. Jóhannesson, A. S. Johnson, T. J. Johnson, W. N. Johnson, T. Kamae, H. Katagiri, J. Kataoka, M. Kerr, J. Knödseder, M. Kuss, J. Lande, L. Latronico, S. Lee, M. Lemoine-Goumard, F. Longo, F. Loparco, B. Lott, M. N. Lovellette, P. Lubrano, G. M. Madejski, A. Makeev, M. N. Mazziotta, P. F. Michelson, W. Mitthumsiri, T. Mizuno, A. A. Moiseev, C. Monte, M. E. Monzani, A. Morselli, I. V. Moskalenko, S. Murgia, M. Naumann-Godo, P. L. Nolan, J. P. Norris, E. Nuss, T. Ohsugi, N. Omodei, E. Orlando, J. F. Ormes, M. Ozaki, D. Paneque, J. H. Panetta, M. Pepe, M. Pesce-Rollins, V. Petrosian, C. Pfrommer, F. Piron, T. A. Porter, S. Profumo, S. Rainò, R. Rando, M. Razzano, A. Reimer, O. Reimer, T. Reposeur, J. Ripken, S. Ritz, A. Y. Rodriguez, R. W. Romani, M. Roth,
  - [55] H. Sadrozinski, A. Sander, P. M. Saz Parkinson, J. D. Scargle, C. Sgrò, E. J. Siskind, P. D. Smith, G. Spandre, P. Spinelli, J. Starck, L. Stawarz, M. S. Strickman, A. W. Strong, D. J. Suson, H. Tajima, H. Takahashi, T. Takahashi, T. Tanaka, J. B. Thayer, J. G. Thayer, L. Tibaldo, O. Tibolla, D. F. Torres, G. Tosti, A. Tramacere, Y. Uchiyama, T. L. Usher, J. Vandenbroucke, V. Vasileiou, N. Vilchez, V. Vitale, A. P. Waite, P. Wang, B. L. Winer, K. S. Wood, Z. Yang, T. Ylinen, and M. Ziegler, *ApJL* **717**, L71 (2010), arXiv:1006.0748 [astro-ph.HE].
- [55] We average the LP DM flux in the energy range 1 – 10 GeV before we compare it to the upper limits.

Only LP models have energetic enough CRe such that IC emission powerful to either constrain or be detected

similar shape for BM continuum models

if CC, then skewed towards large X-ray fluxes; X-ray emission good proxies for gamma-ray emission –) The dust turns up at about a factor 100 lower than the stars –) The other figure show the spectral shape of the IC-star with the same spectral shape as the dust, it shows the same gamma-ray slope as the dust –) The reason

why there is only a factor 10 difference in the break in the gamma-ray emission between the star and dust is related to the KN. In our CRp paper, the last figure shows that at  $E_\gamma = 100 \text{ TeV}$ , the spectra is suppressed with about a factor 10 (also depends on  $\alpha_e$ ). Since the dust photons have a factor 10 higher energy, I expect this suppression at about 10 TeV. For star photons the suppression should be at 100 GeV. So the star photons are definitely KN suppressed, which explains the earlier break and the steeper slope.



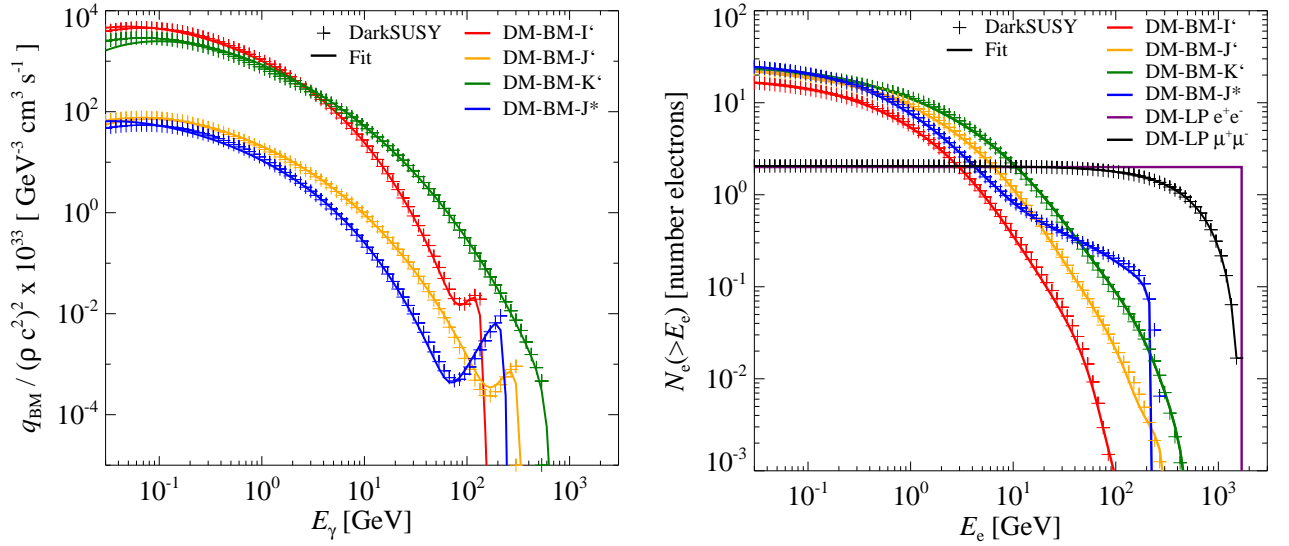


FIG. 18. The underlying source functions for different DM models. Crosses show the simulated data from *DarkSUSY* and the solid lines show the fit to the data using Eq.... LEFT PANEL: normalized differential continuum spectra for four different DM benchmark (BM) models;  $I'$  model (red),  $J'$  (orange),  $K'$  (green), and  $J^*$  (blue). RIGHT PANEL: number of electron and positron per DM annihilation above the electron energy  $E_e$  for different dark matter models;  $I'$  BM model (red),  $J'$  BM model (orange),  $K'$  BM model (green), and  $J^*$  BM model (blue), leptophilic (LP) DM annihilating into electrons and positrons (purple), and LP DM annihilating into muons (black).

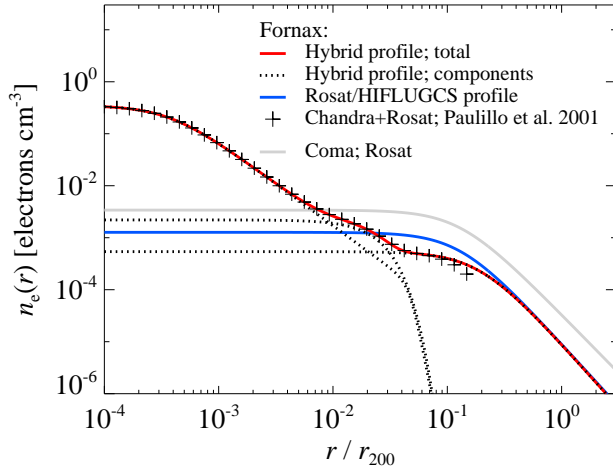


FIG. 19. Comparing different electron number density profiles for the Fornax cluster. Black crosses show the density profile inferred from deprojected Chandra and Rosat X-ray surface brightness observations CITE. The total hybrid profile shown by the red solid line represent the best fit to the data, where the fitted individual density components are shown by the black dotted lines. The blue solid line show the single beta density profile inferred from the HIFLUGCS catalogue. Due to insufficient sensitivity to the outer part in the plotted data, we infer the outer slope found in the HIFLUGCS catalogue.

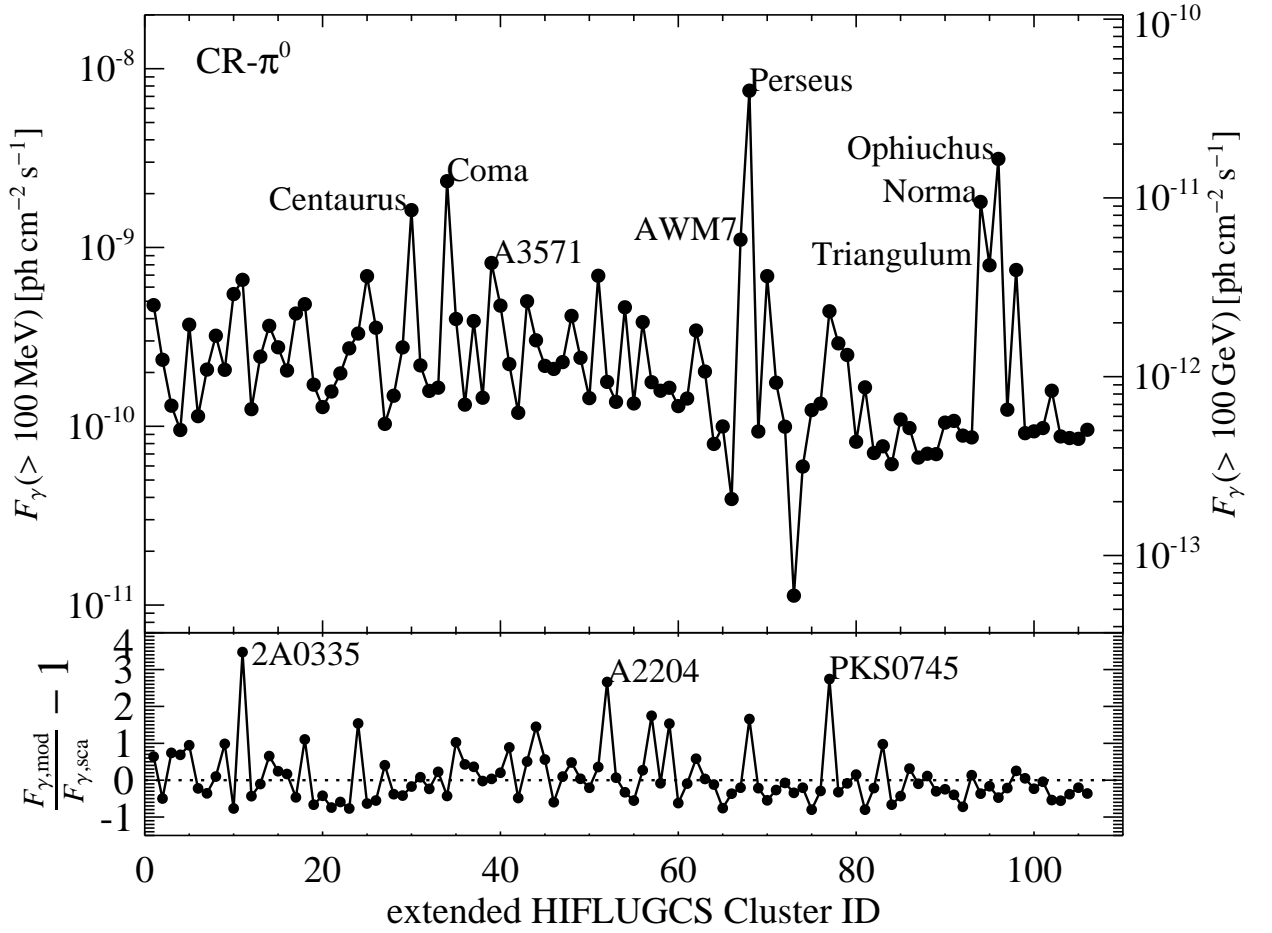


FIG. 20. Comparing the flux from clusters in the extended HIFLUGCS catalogue. We show the energy integrated gamma-ray flux induced by CRps for the 106 clusters included in the extended HIFLUGCS catalogue. The fluxes are calculated within  $r_{200}$ , and are derived using a single beta profile for each cluster's gas density profile (see text for details). The upper panel show the energy integrated flux above 100 MeV (left side) and above 100 GeV (right side), both as a function of HIFLUGCS cluster ID. The name of the eight brightest clusters are written out. The lower panel show the relative difference between the gamma-ray flux predicted by mass-luminosity scaling relations compared to the flux computed using the semi-analytically model [20]. The name of the clusters with the largest offset are printed out, which correlate with cool core clusters.

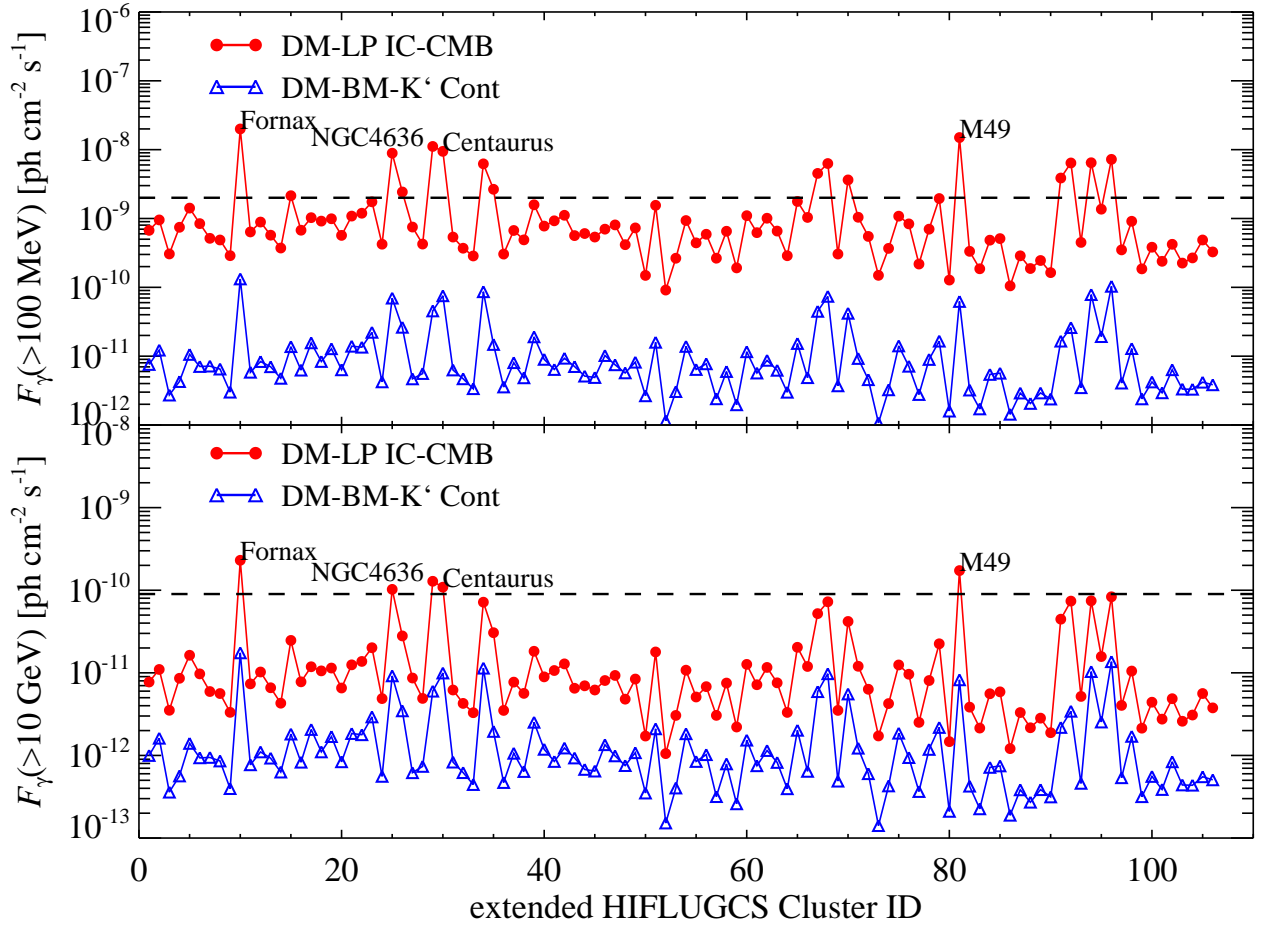


FIG. 21. Comparing the flux from clusters in the extended HIFLUGCS catalogue. We show the energy integrated gamma-ray fluxes derived from both leptophilic DM that result in inverse Compton upscattered CMB photons (red), and the continuum emission from the DM K' benchmark model (blue). The fluxes are calculated within  $r_{200}$  for each of the 106 clusters included in the extended HIFLUGCS catalogue, and are derived using a single beta profile for each cluster's gas density profile (see text for details). The upper panel show the energy integrated flux above 100 MeV and the lower panel above 10 GeV, both as a function of HIFLUGCS cluster ID. The name of the four brightest clusters are written out, where Fornax and M49 are the brightest targets.